Article

Current Biology

Spectral inference reveals principal cone-integration rules of the zebrafish inner retina

Graphical abstract

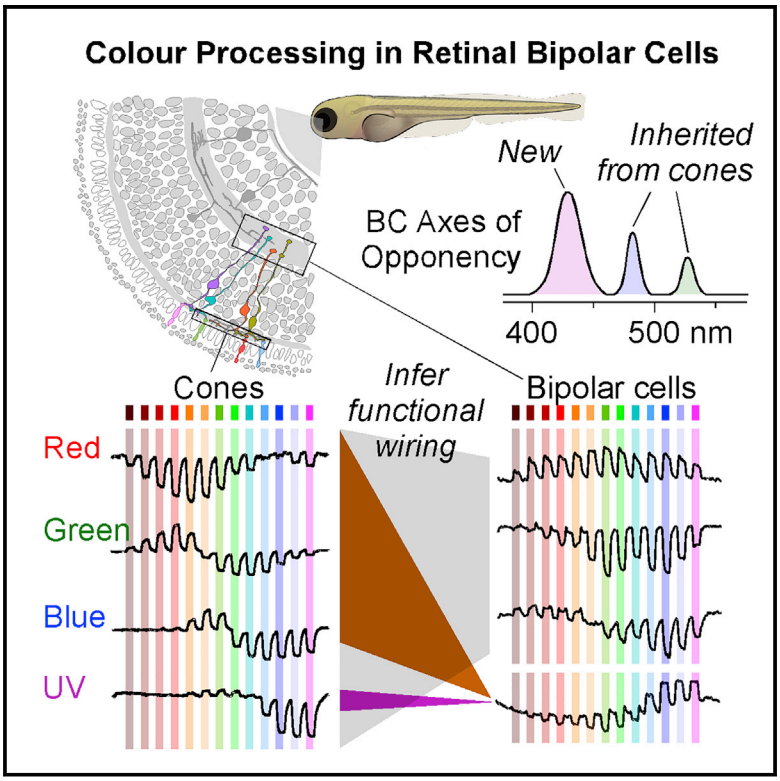

Highlights

- Three axes of spectral opponency are encoded by larval zebrafish bipolar cells
- The two longer wavelength opponent axes are probably inherited from cones
- The short-wavelength opponent axis is probably built in the inner retina
- This third opponent axis may link with S-cone opponent circuit in mammals

Authors

Philipp Bartel, Takeshi Yoshimatsu, Filip K. Janiak, Tom Baden

Correspondence

t.baden@sussex.ac.uk

In brief

Bartel et al. use "spectral circuit mapping" in the tetrachromat zebrafish to link their retinal bipolar cells to cones. This reveals the inner retina's dominant functional integration rules, highlights the existence of three axes of spectral opponency, and suggests a possible evolutionary link between color circuits in fish and mammals.

Bartel et al., 2021, Current Biology *31*, 1–13
December 6, 2021
https://doi.org/10.1016/j.cub.2021.09.047

CellPress

Please cite this article in press as: Bartel et al., Spectral inference reveals principal cone-integration rules of the zebrafish inner retina, Current Biology (2021), https://doi.org/10.1016/j.cub.2021.09.047

Current Biology

CellPress
OPEN ACCESS

Article

Spectral inference reveals principal cone-integration rules of the zebrafish inner retina

Philipp Bartel,[1] Takeshi Yoshimatsu,[1] Filip K. Janiak,[1] and Tom Baden[1,2,3,4,*]
[1]School of Life Sciences, University of Sussex, Biology Road, BN1 9QG Brighton, UK
[2]Institute of Ophthalmic Research, University of Tübingen, Elfriede-Aulhorn-Strasse 7, 72076 Tübingen, Germany
[3]Twitter: @NeuroFishh
[4]Lead contact
*Correspondence: t.baden@sussex.ac.uk
https://doi.org/10.1016/j.cub.2021.09.047

SUMMARY

Retinal bipolar cells integrate cone signals at dendritic and axonal sites. The axonal route, involving amacrine cells, remains largely uncharted. However, because cone types differ in their spectral sensitivities, insights into bipolar cells' cone integration might be gained based on their spectral tunings. We therefore recorded *in vivo* responses of bipolar cell presynaptic terminals in larval zebrafish to widefield but spectrally resolved flashes of light and mapped the results onto spectral responses of the four cones. This "spectral circuit mapping" allowed explaining ~95% of the spectral and temporal variance of bipolar cell responses in a simple linear model, thereby revealing several notable integration rules of the inner retina. Bipolar cells were dominated by red-cone inputs, often alongside equal sign inputs from blue and green cones. In contrast, UV-cone inputs were uncorrelated with those of the remaining cones. This led to a new axis of spectral opponency where red-, green-, and blue-cone "Off" circuits connect to "natively-On" UV-cone circuits in the outermost fraction of the inner plexiform layer—much as how key color opponent circuits are established in mammals. Beyond this, and despite substantial temporal diversity that was not present in the cones, bipolar cell spectral tunings were surprisingly simple. They either approximately resembled both opponent and non-opponent spectral motifs already present in the cones or exhibited a stereotyped non-opponent broadband response. In this way, bipolar cells not only preserved the efficient spectral representations in the cones but also diversified them to set up a total of six dominant spectral motifs, which included three axes of spectral opponency.

INTRODUCTION

For color vision, retinal circuits combine and contrast the signals from spectrally distinct types of photoreceptors.[1] For this, our own trichromatic vision uses spectral signals along two main opponent axes: "blue-yellow" and "green-red."[2–5] Of these, blue-yellow comparisons are based on ancestral cone-type selective retinal circuits that differentially contact SWS1 ("blue") and LWS cones ("green or red" aka "yellow"), while reliably contrasting "green-red" is thought to require the central brain.[1,5–7] This is because primate "green" and "red cones" emerged from a relatively recent LWS gene duplication that enabled new green sensitivity in some LWS cones, however, without providing a known means for postsynaptic retinal circuits to distinguish between green and red LWS-cone variants.[3,8] Accordingly, in our own eyes, one axis of spectral opponency arises in the retina and a second is probably decoded only in the brain.

In contrast, most non-mammalian vertebrate lineages, including fish, amphibians, reptiles, and birds, retain the full complement of ancestral cone types based on four opsin-gene families: SWS1 (UV cones), SWS2 (blue cones), RH2 (green cones), and LWS (red cones).[1,9–11] Each of these four ancestral cones provides type-specific extracellular matrix proteins that developmental programs use to build cone-type selective circuits in the outer retina (e.g., zebrafish[12–14] and chicken[15–17]). Accordingly, in these non-mammalian lineages, the expectation is that up to tetrachromatic color vision should be possible based on stereotyped cone-opponent ancestral circuits that are specified during development, without a necessity for building additional spectral opponencies in the brain. In agreement, physiological recordings from retinal neurons in cone-tetrachromatic species, including turtles[18] and diverse species of fish,[9,19–23] consistently revealed a rich complement of complex spectral signals, including diverse spectral opponencies.

However, what the dominant opponencies are and how they are built at the circuit level remains incompletely understood in any cone-tetrachromat vertebrate.[9] This is in part because already horizontal cells in the outer retina functionally interconnect and potentially retune cone types,[10,14,24–26] thus limiting the possibility of making inferences about spectral processing based on recordings from downstream neurons. To address

Please cite this article in press as: Bartel et al., Spectral inference reveals principal cone-integration rules of the zebrafish inner retina, Current Biology (2021), https://doi.org/10.1016/j.cub.2021.09.047

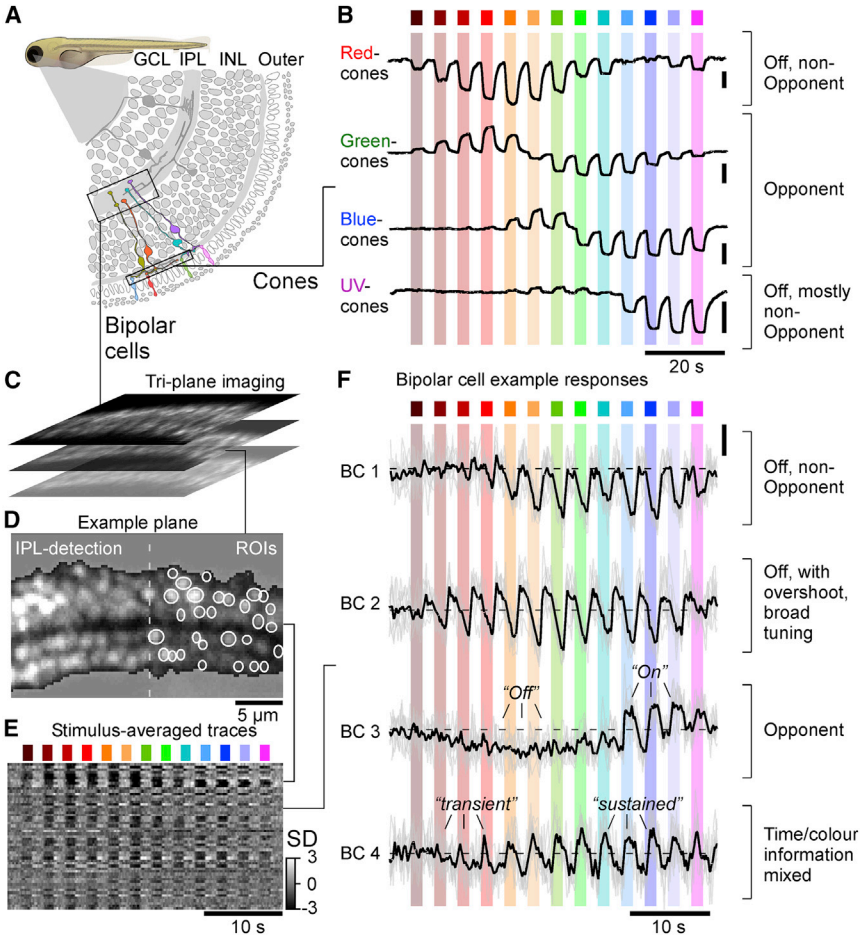

Figure 1. Measuring high-spectral resolution tuning curves in zebrafish bipolar cells

(A) Schematic of the larval zebrafish retina, with cone terminals in the outer retina and bipolar cell (BC) terminals in the inner retina highlighted.

(B) Mean calcium responses of red-, green-, blue-, and UV-cone terminals to a series of 13 spectrally distinct widefield flashes of light as indicated (data from Yoshimatsu et al.[27]). Note that, for clarity, the response to a 14th "low-power-control" UV LED was graphically removed compared to the original publication.

(C–F) Illustration of recording strategy for BC terminals in the inner plexiform layer (IPL) and exemplary results. An optical triplane approach (C, top) was used to simultaneously record from three planes of larval zebrafish BC terminals expressing SyjGCaMP7b by way of two-photon imaging coupled with remote focusing (STAR Methods). From here, we automatically placed regions of interest (ROIs) and detected the boundaries of the IPL (D; STAR Methods). Time traces from all ROIs in a recording plane were *Z* scored and averaged across 3–5 response repeats of the full stimulus sequence (E). Example traces from individuals ROIs (F) are shown as individual repeats (gray) and averages across repeats (black).

Zebrafish larva schematic (A) by Lizzy Griffith. See also Figure S1.

this, we recently measured the *in vivo* spectral tuning of the synaptic outputs from the four cone types in larval zebrafish using spatially widefield but spectrally narrow flashes of light.[27] This revealed that red cones are non-opponent, green and blue cones are strongly opponent with distinct zero crossings (~523 and ~483 nm, respectively), and UV cones are weakly opponent with a zero crossing at ~450 nm. Accordingly, in larval zebrafish, already the cone output provides up to three axes of spectral opponency.[9,27] However, the opponent axis provided by UV cones was weak, which left its role in zebrafish color vision unclear. Moreover, in view of expected extensive mixing of cone signals in downstream circuits,[12,28] whether and how the cones' spectral axes are propagated downstream remains unknown.

Accordingly, we asked how downstream retinal circuits make use of the spectrally complex cone signals to either consolidate or to retune their spectral axes for transmission to the brain. For this, we used two-photon (2P) imaging to measure spatially widefield but spectrally highly resolved tuning functions at the level of retinal bipolar cell (BCs) presynaptic terminals in the inner retina. This strategy was previously used to establish the spectral tunings of the cones,[27,29] thus facilitating direct comparison.

We find that all three spectral axes already set up by the cones are conserved at the level of BC presynaptic terminals, and no new axes are created. However, the "UV red" axis was notably boosted and diversified into numerous variants of either polarity via new opponent circuits that mostly derive from red-, green-, and blue-Off-circuits connecting to UV-On-circuits. The remaining non-opponent BCs were either broadly tuned, likely built by pooling signals from all four cone types, or essentially resembled the tunings of red and/or UV cones in isolation. Beyond spectral tuning, bipolar cells showed a rich complement of temporal features that were absent in cones, which were notably intermixed with spectral information.

Taken together, larval zebrafish BC circuits for color vision therefore directly built upon the existing cone tunings rather than set up fundamentally new opponencies, while at the same time adding substantial temporal complexity to the retinal code.

RESULTS

A complex interplay of spectral and temporal signals among BCs

To establish *in vivo* spectral tuning functions at the level of individual presynaptic terminals of BCs in the inner retina, we imaged light-evoked calcium responses from 6 to 7 days post-fertilization (dpf) RibeyeA:SyjGCaMP7b zebrafish under 2P using established protocols (STAR Methods).[19,30,31] To record from hundreds of individual BC terminals in parallel, we used a non-telecentric triplane imaging approach (STAR Methods).[32] For light stimulation, we used the same system and protocol previously employed to determine cone tunings (Figures 1A and 1B).[27] In brief, light from 13 spectrally distinct LEDs was collected by a collimator after reflecting off a diffraction grating, which served to narrow individual LED spectra reaching the eye.[33] From here, stimuli were presented to

Please cite this article in press as: Bartel et al., Spectral inference reveals principal cone-integration rules of the zebrafish inner retina, Current Biology (2021), https://doi.org/10.1016/j.cub.2021.09.047

the fish as widefield but spectrally narrow flashes of light (1.5 s On, 1.5 s Off, starting from red and sweeping toward UV; STAR Methods). One example recording from BC terminals is illustrated in Figures 1C–1E alongside averaged cone responses to the same stimulus (Figure 1B) taken from Yoshimatsu et al.[27] In short, each recording plane was automatically processed to detect the boundaries of the inner plexiform layer (IPL) (Figure 1D, left) and to place regions of interest (ROIs) based on pixelwise response coherence over consecutive repeats (Figure 1D, right; STAR Methods). From here, fluorescence traces from each ROI were extracted, detrended, *Z* scored, and averaged over typically 7 to 8 stimulus repetitions (Figures 1D and 1E). This revealed a great diversity in both the spectral and the temporal composition of responses among BCs. For example, some ROIs were entirely non-opponent but differed in their spectral tuning and in the degree to which they "overshot" the baseline between stimulus presentations (Figure 1F, compare ROIs labeled BC1 and BC2). Other ROIs, such as the one labeled BC3, were spectrally opponent, here exhibiting Off signals to mid-wavelength stimulation but On signals to UV stimulation. Finally, some ROIs, including the one labeled BC4, exhibited different temporal responses to long- and short-wavelength stimulation.

Because stimuli were always presented in spectral sequence, which might cause systematic adaptation, we also performed a small number of control experiments with a reduced stimulus set, where we directly compared responses of the same ROIs to ordered and to pseudorandomized stimulus sequences (Figures S1A–S1G). This showed that both approaches gave very similar responses, suggesting that spectral adaptation was not a major feature in our recordings. We recorded responses from a total of n = 72 triplane scans in n = 7 fish, across four major regions of the eye: acute zone (AZ); dorsal (D); nasal (N); and ventral (V). From here, n = 6,125 ROIs ($n_{AZ,D,N,V}$ = 2,535, 1,172, 1,889, and 529, respectively) that passed a minimum response quality criterion (STAR Methods) were kept for further analysis. Next, we clustered BC responses using a mixture of Gaussian models as described previously (STAR Methods).[19,22,34,35] This yielded 29 functional BC clusters (Figures 2A and 2B), here arranged by their mean stratification position in the IPL (Figure 2C). Whether and how this relatively large number of functional BC clusters maps onto veritable BC "types"[28] remains unknown. For comparison, previous studies described 25 functional[19] and 21 anatomical[12] BCs; however, a deeper census of zebrafish BC types, for example, based on additional data from connectomics[36] and/or transcriptomics,[37] remains outstanding.

Consistent with previous work that was based on a different stimulus with lower spectral resolution,[19] zebrafish BC clusters were highly diverse, and many exhibited a regional bias to one or multiple parts of the eye (Figure 2D). For example, several UV-dominated clusters showed a clear regional bias to the acute zone (e.g., $C_{21,25}$) and/or the ventral retina (e.g., $C_{6,27}$), while many broadband clusters were distributed approximately homogeneously across the eye, except ventrally (e.g., $C_{2,5}$). However, with our current focus on BC-spectral tunings, we did not further analyze this eye-wide regionalization.

Overall, BC clusters differed strongly in their wavelength selectivity. For example, clusters C_1 and C_2 both hyperpolarized in response to all tested wavelengths, but C_2 was tuned broadly while C_1 exhibited a notable dip in response amplitudes at intermediate wavelengths. Other clusters exhibited clear spectral opponency. For example, clusters $C_{26–29}$ all switched from Off responses to long-wavelength stimulation to On responses at shorter wavelengths. A single cluster (C_7) exhibited a spectrally triphasic response. BCs also differed in their temporal responses. For example, while cluster C_2 consistently responded in a sustained manner, cluster C_3 responses were more transient and overshot the baseline between light flashes. Finally, diverse spectral and temporal response differences did not only exist between BC clusters but also within. For example, cluster C_6 switched from transient responses during long-wavelength stimulation to sustained responses during short-wavelength stimulation. In some cases, such intermixing of spectral and temporal encoding in a single functional BC cluster could be quite complex. For example, cluster C_{21} switched from small transient On-Off responses via intermediate amplitude transient-sustained On responses to large-amplitude sustained-only On responses in a wavelength-dependent manner.

Overall, in line with connectivity[12,38] and previous functional work, both the spectral[19,22,23] and the temporal diversity[19,22,23,30,39,40] of larval zebrafish BCs long exceeded that of the cones, which at the level of presynaptic calcium were generally sustained[27] and which only exist in four spectral variants (cf. Figure 1B).

Linear cone combinations using four temporal components can account for BC responses

We next explored whether and how these BC cluster means (Figure 2B) could be explained based on cone responses (Figure 3; cf. Figure 1B).[27] For this, we implemented a simple linear model (STAR Methods) based on the following considerations.

BCs may receive cone inputs by two main, non-mutually exclusive routes: directly via dendritic contacts onto cone pedicles in the outer retina and indirectly via lateral inputs from amacrine cells in the inner retina.[28] A third route, via horizontal cells, has been proposed in the case of mice.[41] Whether such a route exists in zebrafish remains unknown.

In the outer retina, direct cone inputs are based on BC-type-specific expression of glutamate receptor and/or transporter variants that are thought to be either all sign conserving or all sign inverting but apparently never a mixture of both.[28,42] Accordingly, dendritic inputs alone should only be able to produce spectral tuning functions in BCs that can be explained by same-sign cone inputs. Any BC that cannot be explained in this manner is then expected to require spectrally distinct inputs from amacrine cells. On the other hand, variations to the temporal structure of a given cones' contribution to a BC's response could be implemented via either route[28,35,43]—that is, via a combination of dendritic and/or axonal inputs. Accordingly, we reasoned that, for a linear transformation, each cone type may feed into a functional BC type via a unique temporal profile that represents the sum of all routes from a given cone to a given BC. In this way, our model effectively sought to explain each BC cluster as a weighted sum of four spectral cone tunings, but each of these four cone inputs could have a unique temporal structure.

To capture the above considerations in a linear model, we combined the four-cone spectral tuning functions (Figure 3A; cf. Figure 1B) with four dominant temporal components extracted from BC responses: light transient; light sustained;

Please cite this article in press as: Bartel et al., Spectral inference reveals principal cone-integration rules of the zebrafish inner retina, Current Biology (2021), https://doi.org/10.1016/j.cub.2021.09.047

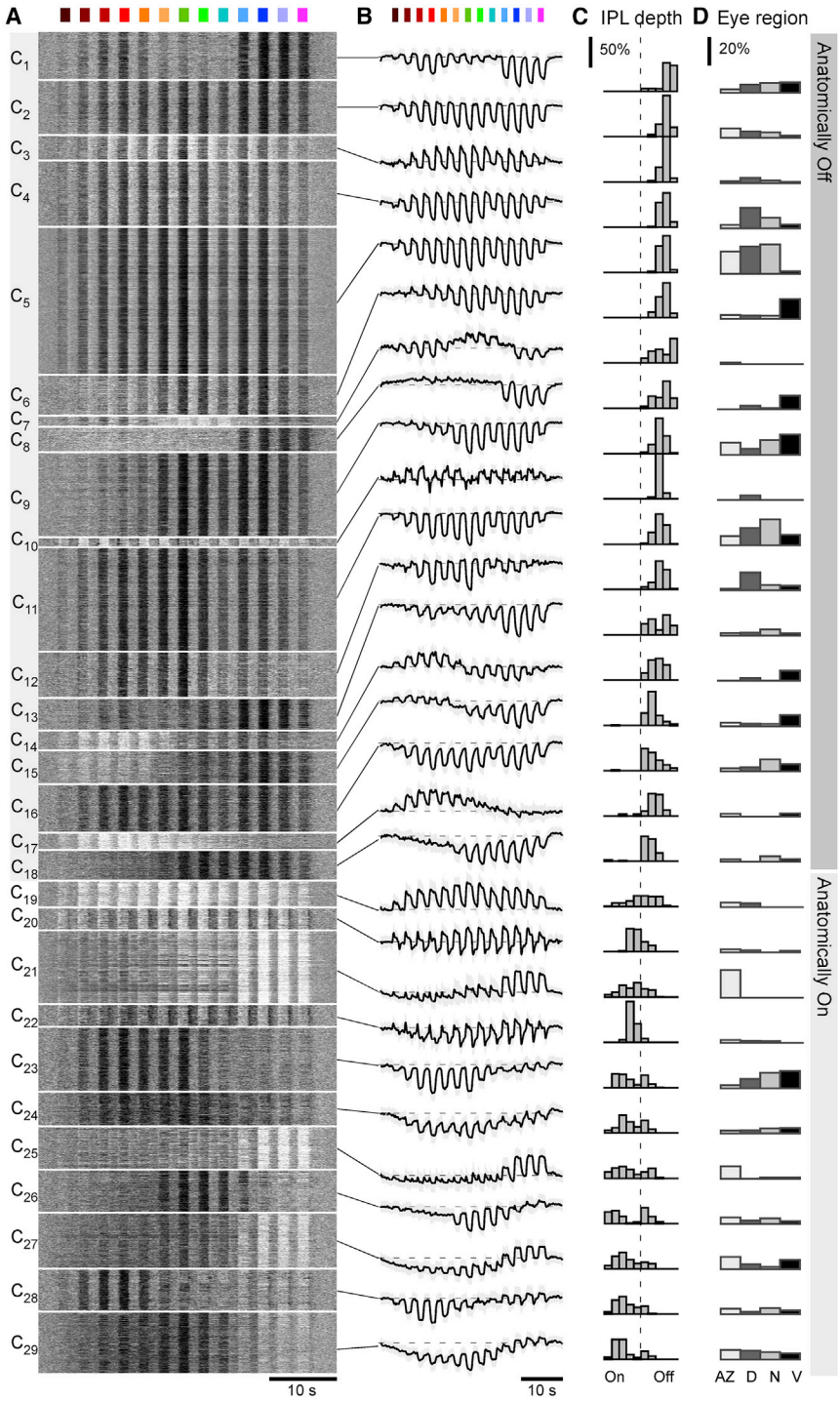

Figure 2. Clustering into 29 functional BC types

Overview of the result from unsupervised clustering of all BC data recorded as shown in Figure 1 that passed a minimum quality index (QI) (QI > 0.4; STAR Methods). For each cluster, shown are the individual BC mean responses as heatmaps (A); the corresponding cluster means and SD shadings, with approximate baseline indicated in dashed (B); distribution of ROI positions in the IPL (C); and each cluster's distribution across the four recording regions within the eye (D, from left: acute zone; dorsal; nasal; and ventral). Histograms in (C) are area normalized by cluster and in (D) by recording region. Clusters are ordered by their average anatomical position in the IPL, starting from the border with the inner nuclear layer (cf. C). The colored symbols indicate the overall spectral group as assigned later (cf. Figures 5F–5K).

dark transient; and dark sustained (Figure 3B; STAR Methods). We restricted the model to capture the central ten light stimuli (i.e., omitting the first two red flashes and the last UV flash) where BC clusters generally exhibited the greatest response diversity (Figure 2).

Notably, in the following paragraphs, we avoid the use of the common shorthand "On" or "Off" because, in view of spectral opponency already present in cones,[27] a sign-conserving input to a BC is not categorically Off, and vice versa, a sign-inverting input is not categorically On. Instead, we use the terms "light" and "dark" response, in reference to a response that occurs in the presence or absence of a light stimulus, respectively. Also note that all extracted spectral tuning functions (e.g., Figure 3A) are x-inverted compared to the time axes in recordings and reconstructions (e.g., Figures 3D and 3E). This was done because recordings were performed from long- to short-wavelength stimuli, but spectral tuning functions are conventionally plotted from short to long wavelengths. Weights were scaled such that the mean of their magnitude equaled one, with weights <0.5 ("near-zero") excluded from the summary plots for visual clarity. Full weights, including a detailed overview of each cluster, are available in Data S1.

Figures 3C–3E illustrate the intermediate steps (Figures 3C and 3D) and final output (Figure 3E) of the model for example cluster C_{22}. This functional BC type was broadly tuned but switched from transient responses to long-wavelength stimulation to more sustained responses at shorter wavelengths (Figure 3E, gray trace; cf. Figures 2A and 2B). To capture this behavior (Figure 3E, black trace), the model drew on all four cones (Figure 3C), however, with a particularly strong sign-conserved contribution from red cones (Figure 3C, left). Here, the model placed a strong sign-conserving weight onto the dark-transient (D_{tr}) component of the red cone (Figure 3D, left, third trace). The strength and sign of this weight is illustrated in Figure 3C (third downward-facing red bar). In addition, the model also placed weaker sign-conserving weights onto the dark-sustained

Please cite this article in press as: Bartel et al., Spectral inference reveals principal cone-integration rules of the zebrafish inner retina, Current Biology (2021), https://doi.org/10.1016/j.cub.2021.09.047

CellPress
OPEN ACCESS

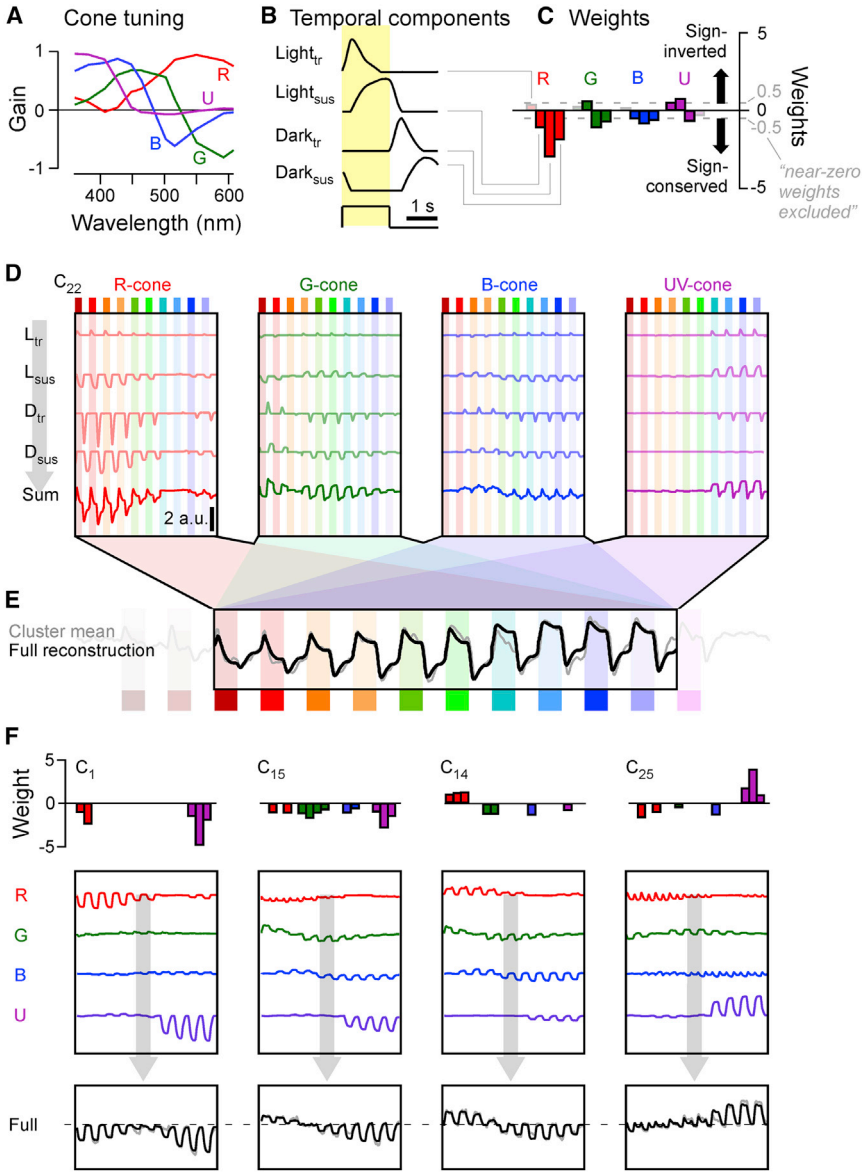

Figure 3. Reconstructing bipolar cell responses from cones

(A–E) Summary of the reconstruction strategy for example cluster C_{22} (for details, see STAR Methods). Each BC-cluster reconstruction is based on the linear combination of the spectral tuning functions of the four cone types (A; from Yoshimatsu et al.[27]) with four stereotyped temporal components associated with individual light flashes (B), yielding 4 × 4 = 16 weights (C). Weights are shown in blocks of temporal component weights (from left: light transient; light sustained; dark transient; and dark sustained) associated with each cone (indicated by the corresponding colors). Bars above zero indicate sign-inverted ("On") weights, while bars below zero indicate sign-conserved ("Off") weights. The corresponding full expansion of this reconstruction is shown in (D). Individual combination of each cone's tuning function (A) with each temporal component (B), scaled by their corresponding weight (C), yields sixteen "sub-traces" (D; upper four traces in each of the four panels, labeled L_{tr}, L_{sus}, D_{tr}, and D_{sus}). Summation of each cone's four sub-traces yields that cone's total contribution to the cluster (D, bottom traces, labeled "sum"). Finally, summation of the four cone totals yields the full reconstruction (E, black trace), shown superimposed on the target cluster mean (gray).

(F) As (A)–(E) but showing only the weights (top), cone totals (middle), and full reconstructions (bottom) for another four example clusters (from left: C_1; C_{15}; C_{14}; and C_{25}).

Further detail on reconstructions is shown in Figure S2, and all clusters' individual results are detailed in Data S1.

(Figure 3D, left, fourth trace) and light-sustained (second trace) components and a weak sign-inverted weight onto the dark-transient component (first trace). Summation of these four kinetic components yielded the total modeled red cone contribution to this cluster (Figure 3D, bottom trace).

The same principle was applied across the remaining three cones, yielding a total of sixteen (four cones times four temporal components) weights per cluster (cf. Figure 3C). In the example presented, weights were mostly sign conserving (facing downward). However, to capture the relatively complex temporal dynamics of this cluster, which systematically overshot the baseline between flashes, the model also drew on a number of weaker sign-inverted weights (facing upward), for example, for all light-transient components.

Figure 3F illustrates mean outputs of the model for another four example clusters with diverse spectral and temporal behaviors. Of these, the spectrally bimodal but "temporally simple" response profile of C_1 was well approximated by all sign-conserving inputs from red and UV cones (Figure 3F, left). Similarly, the spectrally opponent behavior of C_{15} could be captured by all-sign-conserving inputs from all four cones (Figure 3E, second panel). Accordingly, as expected from the cone tunings, generating opponent responses at the level of BC terminals does not categorically require new sign opposition in the inner retina—instead, the opponency can simply be inherited from the cones. Nevertheless, not all opponent BC responses could be explained in this manner. For example, opponent cluster C_{14} required sign-inverted inputs from red cones but sign-conserving inputs from green, blue, and UV cones (Figure 3E, third panel). Finally, even the more complex spectral and temporal BC clusters could be well approximated by relatively simple cone mixtures. For example, C_{25} was captured by combining sign-conserved light- and dark-transient inputs from red and blue cones with mostly sustained and sign-inverted inputs from UV cones (Figure 3E, rightmost).

Overall, this linear fitting procedure captured ~95% of the total variance across the 29 cluster means (Figure S2A; STAR Methods). Similarly, the fits also captured ~95% of the temporal detail, based on comparison of the mean power spectra of the

Please cite this article in press as: Bartel et al., Spectral inference reveals principal cone-integration rules of the zebrafish inner retina, Current Biology (2021), https://doi.org/10.1016/j.cub.2021.09.047

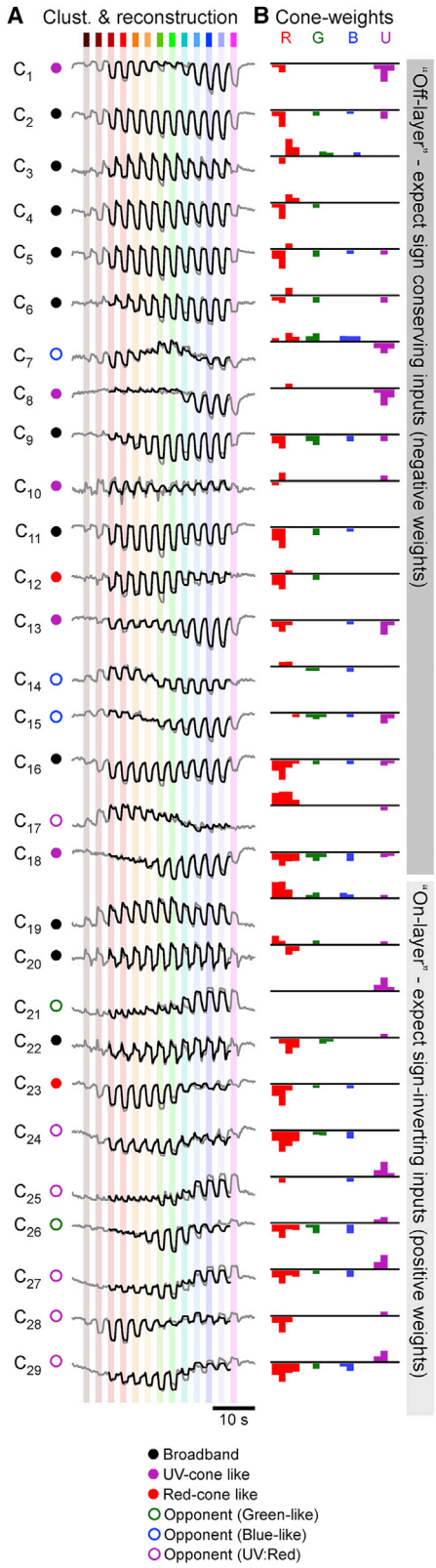

Figure 4. A functional overview of cone bipolar cell mappings

Overview of all BC-cluster means (A, gray traces; cf. Figure 2B) and their full reconstructions based on the strategy detailed in Figure 3 (black traces). Associated weights are shown in (B). For clarity, "near-zero" weights (abs(w) < 0.5) are omitted. Full weights are shown in Data S1. Note that, based on outer retinal inputs only, weights are generally expected to be sign conserving for clusters in the traditional Off layer (C_1–C_{18}) and sign inverting in the anatomical On layer (C_{19}–C_{29}), as indicated on the right. The round symbols plotted next to each cluster (A) denote their allocated spectral group, as detailed in Figures 5F–5K and associated text.

cluster means and that of the residuals (Figure S2B; STAR Methods). The full result of this process is summarized in Figure 4, each time showing the cluster mean (gray) and reconstruction (black) alongside weight summaries per cone following the schema illustrated in Figures 3B and 3C. Further detail is shown in Data S1.

Based on the traditional separation of the inner retina into "Off" and "On layers,"[28] we may correspondingly expect mainly sign-conserving (negative) weights in "Off-stratifying" clusters C_1–C_{18} and mainly sign-inverting (positive) weights for "On-stratifying" clusters C_{19}–C_{29}. However, this expectation was not met in several cases, for example, for most of the On-stratifying clusters that nevertheless showed a general abundance of negative (Off) weights for red-, green-, and blue-cone inputs. From here, we next explored the general rules that govern overall cone-signal integration by BCs.

The inner retina is dominated by red-cone inputs

First, we computed histograms of all weights per cone (Figure 5A) and per temporal component (Figure 5B) to determine the dominant input motifs across the population of all BCs. This revealed that, overall, the amplitudes of red-cone weights tended to be larger than those of all other cones (red absolute weights W_R = 1.82 ± 1.22; $W_{G,B,U}$ = 0.68 ± 0.47, 0.62 ± 0.45, and 0.87 ± 0.88, respectively, range in SD; $p < 0.001$ for all red combinations; Wilcoxon rank-sum test). This red dominance was stable also when the four eye regions were analyzed separately ($p < 0.001$ in each case). Similarly, light-response component weights tended to be larger than dark-response component weights ($W_{LT,\ LS,\ DT,\ DS}$ = 0.94 ± 0.75, 1.73 ± 1.20, 0.85 ± 0.8, and 0.48 ± 0.54, respectively; Figure 5B). Here, the light-sustained response components that already dominate the cones (cf. Figure 1B) remained largest overall also in BCs ($p < 0.001$ for all $Light_{sus}$ combinations; Wilcoxon rank-sum test).

Red-, green-, and blue-cone weights co-vary independent of UV-cone weights

Next, we explored the weight relationships between the four cone types across clusters. In general, a strong correlation between weights attributed to any two cone types would suggest that inputs from these cones tend to be pooled, for example, by the dendrites of individual BCs contacting both cone types. In contrast, a low correlation or even anticorrelation between cone weights could indicate the presence of cone opponency.

Across clusters, we found that red-cone weights strongly correlated the weights of both green (ρ = 0.73; 95% confidence intervals [CI] 0.49 and 0.86; Figure 5C) and blue cones (ρ = 0.87, CI 0.74 and 0.94, Figure 5D; green versus blue: ρ = 0.89; CI 0.77 and 0.95; cf. Figure S3A). The tight association between red-, green-, and blue-cone weights extended across both the all-sign-inverting (bottom left) and the all-sign-conserving (top right)

Please cite this article in press as: Bartel et al., Spectral inference reveals principal cone-integration rules of the zebrafish inner retina, Current Biology (2021), https://doi.org/10.1016/j.cub.2021.09.047

CellPress
OPEN ACCESS

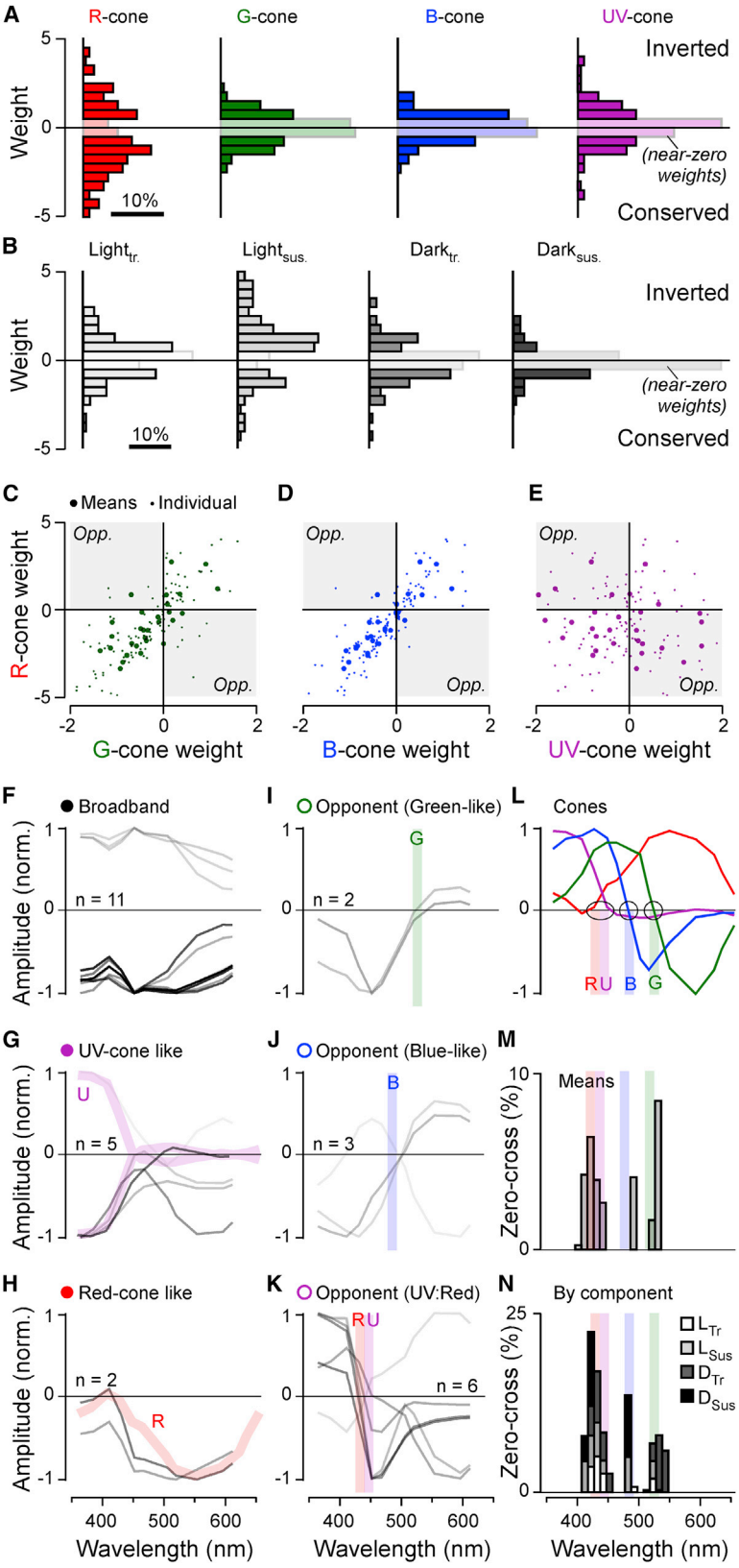

Figure 5. Major trends in cone weights and spectral tunings

(A and B) Histograms of all weights associated with inputs to each of the four cones across all clusters, independent of temporal-component types (A) and, correspondingly, histograms of all weights associated with temporal components, independent of cone type (B). Near-zero weights (abs(w) < 0.5) are graphically de-emphasized for clarity. All weights contributed equally to these histograms, independent of the size of their corresponding cluster.

(C–E) Scatterplots of all clusters' weights associated with each cone plotted against each other as indicated. Large symbols denote the mean weight associated with each cone and cluster across all four temporal components (i.e., one symbol per cluster), while small symbols denote each weight individually (i.e., four symbols per cluster, corresponding to L_{tr}, L_{sus}, D_{tr}, and D_{sus}). The remaining three possible cone correspondences (G:B, G:U, and B:U) are shown in Figures S3A–S3C.

(F–K) Peak-normalized "bulk" spectral tuning functions of all 29 clusters, grouped into six categories as indicated. The strength of each line indicates the numerical abundance of ROIs belonging to each cluster (darker shading = larger number of ROIs; exact number of ROIs contributing to each cluster are listed in Data S1). As appropriate, spectral tuning functions of cones (cf. L) are shaded into the background, as appropriate (G and H, thick colored traces) to illustrate the close spectral correspondences of associated cones and BCs. Similarly, for three spectrally opponent groups (I and K), the approximate positions of the corresponding cone's zero crossings are indicated with a vertical shaded line (cf. L).

(L) Cones' spectral tuning functions, with approximate zero crossings (blue and green cones) and zero positions (red and UV cones) graphically indicated.

(M and N) Histograms of zero crossings across all BC clusters, incorporating the abundance of ROIs belonging to each cluster. Shown are crossings of bulk spectral tunings functions (M; cf. F–H) and of spectral tuning functions that were computed for each temporal component individually, as indicated (see also Figures S3F–S3I and Data S1). Note the three prominent peaks of zero-crossing positions, approximately aligned with the zero positions and crossings of the cones. These peaks largely disappeared when time components were fully randomized (Figure S3D) or randomly permuted across cones (Figure S3E).

Please cite this article in press as: Bartel et al., Spectral inference reveals principal cone-integration rules of the zebrafish inner retina, Current Biology (2021), https://doi.org/10.1016/j.cub.2021.09.047

quadrants and comprised few exceptions in the two remaining quadrants that would indicate cone opponency. Accordingly, zebrafish BCs did not tend to differentially combine inputs from red, green, or blue cones of either polarity to set up potentially new opponent axes.

In contrast, red-cone weights were uncorrelated with UV-cone weights ($\rho = -0.21$, CI −0.55 and 0.14, Figure 5E; green sc. UV: $\rho = -0.04$, CI −0.40 and 0.34; blue versus UV; $\rho = -0.34$, CI −0.63 and 0.03; Figures S3B and S3C), with many clusters scattering across the two sign-opponent quadrants (i.e., top left and bottom right). Accordingly, reconstructing a substantial fraction of BC clusters required opposite sign inputs from red, green, and blue versus UV cones, suggestive of a newly set up form of spectral opponency in the inner retina. Interestingly, in some cases, a cluster could exhibit small Off responses in the UV range despite using sign-inverting weights for UV cones (e.g., C_{23}—best seen in Data S1). This was possible because all cones respond to UV light to some extent (Figure 1B). In some cases, the sum of inferred red-, green-, and blue-cone inputs could then outweigh inferred UV-cone inputs. We next explored the spectral tuning of BC clusters in further detail.

BC spectral responses fall into three opponent and three non-opponent groups

The complex interplay of temporal and spectral structure in BC responses (Figure 2) meant that their spectral tuning functions could not easily be extracted directly from the BC-cluster means, for example, by means of taking the area under the curve in response to each flash of light. Instead, we estimated their tuning functions based on their fitted cone weights (cf. Figure 4). To this end, for each cluster, we summed sixteen cone-tuning functions (based on Figure 3A), each scaled by the cluster's associated sixteen weights (i.e., red-L_{tr} + red-L_{sus}.+ red-$D_{tr.}$ and so on). This summarized each cluster's "bulk" response in a single spectral tuning function that gave equal weight to each of the four temporal components (Figures 5F–5K). By this measure, 18 of the 29 BC clusters were non-opponent (62%; Figures 5F–5H) and 11 were opponent (38%; Figures 5I–5K). Here, opponency was defined as any tuning function that crossed and overshot zero at least once, with an amplitude of at least 10% compared to that of the opposite (dominant) polarity peak response.

Non-opponent clusters ("closed" symbols; cf. Figure 4A) approximately adhered to three major groups: spectrally broad (three On and eight Off clusters; Figure 5F); approximately UV cone like (one On and four Off clusters; Figure 5G); and approximately red cone like (two Off clusters; Figure 5H). Similarly, opponent clusters ("open" symbols) fell into three major groups based on the spectral positions of their zero crossings: two green-cone-like clusters (both $short_{Off}/long_{On}$, crossing at 520 and 536 nm; Figure 5I); three blue-cone-like clusters (two $short_{Off}/long_{On}$, crossing at 497 and 499 nm, plus the single triphasic C_7 with a dominant $short_{On}/long_{Off}$ zero crossing at 490 nm; Figure 5J); and six UV-cone versus red-, green-, and blue-cone opponent clusters (henceforth: UV:R/G/B; five $short_{On}/long_{Off}$, crossing at 416, 425, 428, 435, and 448 nm; one $short_{Off}/long_{On}$, crossing at 438 nm; Figure 5K). In comparison, green- and blue-cone zero crossings, respectively (Figure 5L; from Yoshimatsu et al.[27]), occurred at ~523 and ~483 nm, while red and UV cones, respectively, approached zero between ~425 and 450 nm (Figures 5I–5N, shadings).

The tight correspondence between opponent BC clusters (Figures 5I–5K) and cone tunings (Figure 5L) was further illustrated by the histogram of BC zero crossings that also incorporated relative abundances of ROIs contributing to each cluster (Figure 5M). The histogram showed three clear peaks that were well aligned to the three spectral axes set up in the cones (shadings). Further, the histogram also retained its overall shape when the four temporal components underpinning each cluster were considered individually (Figure 5N). As a control, this trimodal structure disappeared when component weights were iteratively randomized (Figure S3D) or when temporal components were randomly shuffled between cones (Figure S3E), suggesting that the measured BC tunings emerged from non-random effective cone inputs. In support, and despite appreciable diversity, the spectral tuning functions of the four temporal components that contributed to a given cluster tended to be positively correlated among both opponent and non-opponent clusters (Figures S3F–S3I).

Remarkably, therefore, it appears that, by and large, BCs tended to retain many of the dominant spectral properties of the cones rather than build fundamentally new spectral axes—all despite integrating across multiple cone types and presumably diverse inputs from spectrally complex ACs.[23] The only two notable deviations from this observation were a highly stereotypical spectral broadening in 11 clusters (Figure 5F), which may be linked to outer retinal cone pooling,[12] and, strikingly, the emergence of six strongly UV:R/G/B opponent clusters (Figure 5K).

UV cone, but not red-, green-, and blue-cone weights, follows traditional IPL On-Off lamination

Finally, we asked where the inferred new form of UV:R/G/B opponency might be set up in the inner retina (Figure 6). To this end, we combined the cone-weight data (Figure 4) with information about each BC-terminal's stratification depth within the IPL (Figure 3C). In general, the IPL of all vertebrates studied to date is dominated by "Off circuits" in the upper strata, adjacent to the somata of BCs and most amacrine cells, and by "On circuits" in the lower strata, adjacent to the somata of retinal ganglion cells.[28] Accordingly, light components L_{tr} and L_{sus} are expected to mostly exhibit sign-conserving weights in the upper strata and mostly sign-inverting weights in the lower strata (Figure 6A). Dark components D_{tr} and D_{sus} are expected to exhibit the reverse distribution (Figure 6B).

This textbook expectation, here graphically indicated by dashed lines, was indeed approximately met when considering dark components (Figure 6B—note that UV-dark component weights were generally small and not further considered) and for light components of UV cones (Figure 6A, bottom panel). Similarly, this classical IPL organization was also met by red-, green-, and blue-cone weights for the upper two-thirds of the IPL, which included the traditional Off layer and the upper part of the traditional On layer (Figure 6A, top three panels). However, specifically for red, green, and blue cones, the lower third of the traditional On layer was dominated by weights of the "wrong" polarity (Figure 6A, top three panels). In agreement, most UV:R/G/B opponent clusters stratified in this lower third of the

Please cite this article in press as: Bartel et al., Spectral inference reveals principal cone-integration rules of the zebrafish inner retina, Current Biology (2021), https://doi.org/10.1016/j.cub.2021.09.047

CellPress
OPEN ACCESS

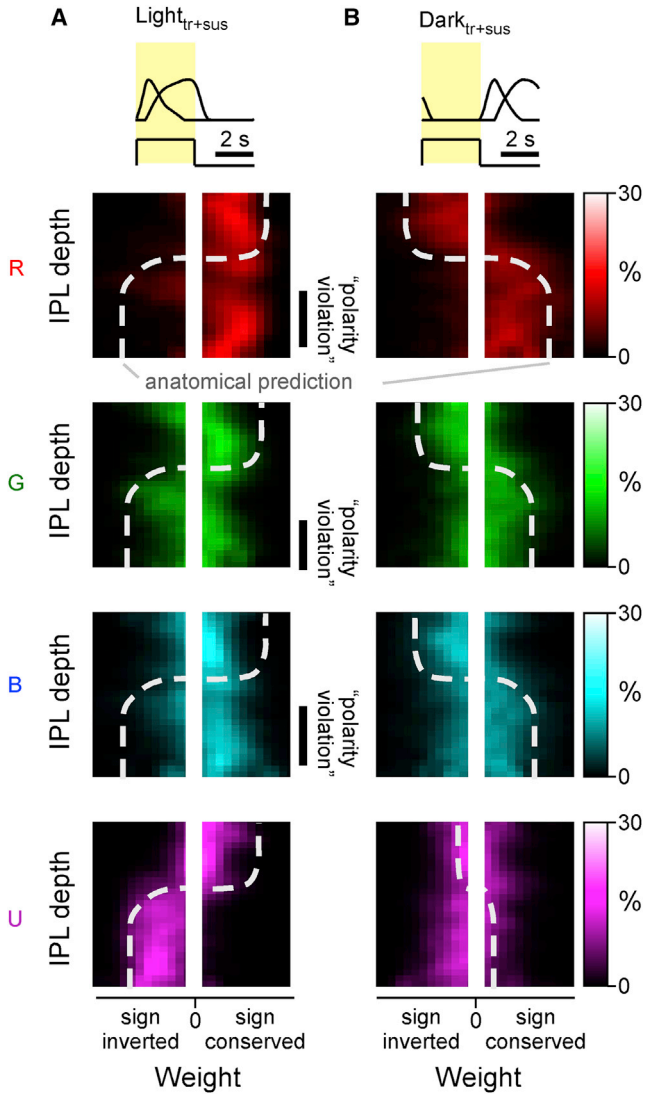

Figure 6. Cone-weight distribution across the inner plexiform layer

Two-dimensional histograms of weights (x axes) associated with each cone resolved by IPL position (y axes). Brighter colors denote increased abundance. For simplicity, the weights associated with the light (L_{tr} and L_{sus}) and dark components (D_{tr} and D_{sus}), are combined in (A) and (B), respectively. Moreover, near-zero weights are not shown (central white bar in all panels). The thick white dotted lines indicate approximate expected distribution of weights based on traditional "On-Off" lamination of the inner retina. By each panel's side, instances where this expectation is violated are highlighted as "polarity violation."

IPL (Figures 3C and 4). Together, this suggests that several of these UV:R/G/B clusters are derived from sign-reversed red-, green-, and blue-cone inputs onto "native" UV-On BCs, for example, by way of amacrine cells.

DISCUSSION

We have shown that the substantial spectral and temporal diversity of larval zebrafish BCs (Figures 1 and 2; cf. Zimmermann et al.[19] and Rosa et al.[30]) can be well captured by a linear combination of inputs from the four spectral cone types (Figures 3 and 4). This in turn allowed us to explore the major functional connectivity rules that govern spectral and temporal widefield signal integration by BCs: we find that red cones overall provide the dominant input to BCs, often complemented by weaker but same-sign inputs from green and blue cones (Figures 5A, 5C, and 5D). Likely as one consequence, BC pathways do not generally set up new axes of spectral opponency in the mid- to long-wavelength range. Rather, they mostly either conserve and diversify the two major opponent motifs already present in the cones (Figures 5I and 5J) or establish non-opponent circuits (Figures 5F–5H). In contrast, inner retinal UV-cone pathways appear to be organized essentially independently to those of red, green, and blue cones (Figure 5E). This leads to the consolidation of a third axis of spectral opponency, contrasting long- and mid-wavelength signals against UV (Figure 5K). This third axis appears to mainly stem from a systematic polarity reversal of inputs from red, green, and blue cones onto "natively-UV-On" BCs in the lower IPL (Figure 6A).

Building spectrally opponent BCs

Because spectral opponency is a prominent feature in larval zebrafish cones,[27] BCs may inherit this property rather than set up new opponent spectral axes by way of ACs. Indeed, the opponency observed in BC cluster C_{15} could be explained based on weighted but all-sign-conserving inputs from all four cones (Figure 4). However, the full picture may be more complex. For example, like C_{15}, cluster C_{14} was also opponent, albeit with a stronger long-wavelength response, and in this case, the model used weakly sign-inverted red-cone weights alongside sign-conserved green- and blue-cone weights. In fact, most UV:R/G/B opponent clusters (e.g., $C_{25–29}$) required opposition of long- versus short-wavelength cone inputs in the inner retina. This hints that inner retinal circuits may generally use a "mix-and-match" strategy to achieve diverse spectral responses by any available route, rather than strictly adhering to any one strategy. This notion is also tentatively supported by the presence of spectrally diverse amacrine cell circuits in adult zebrafish.[23] More generally, it perhaps remains puzzling how the complex interplay of cone pooling in the outer retina with AC inputs in the inner retina, across 29 highly diverse functional BC types that presumably express diverse receptors and ion channels,[28] can ultimately be summarized in a functional wiring logic that, for the most part, simply sums all four cones or "at best" opposes a red, green, and blue system against UV. Resolving this conceptual conflict will likely require targeted circuit manipulations, for example, by comparing BC spectral tunings in the presence and absence of amacrine cell inputs or after targeted cone-type ablations.

Beyond "classical" opponency, several clusters—both opponent and non-opponent—in addition encoded a notable mixture of spectral and temporal information. Interestingly, several of these clusters appeared to be concentrated around the center of the IPL (e.g., $C_{20–25}$; Figures 2B and 2C)—a region that also in mammals has been associated with both transient and sustained processing.[35,44–46] In zebrafish, a mixed time-color code was previously described for the downstream retinal ganglion cells,[22] which now raises the question to what extent ganglion cells may inherit this property from BCs. Moreover, whether

Please cite this article in press as: Bartel et al., Spectral inference reveals principal cone-integration rules of the zebrafish inner retina, Current Biology (2021), https://doi.org/10.1016/j.cub.2021.09.047

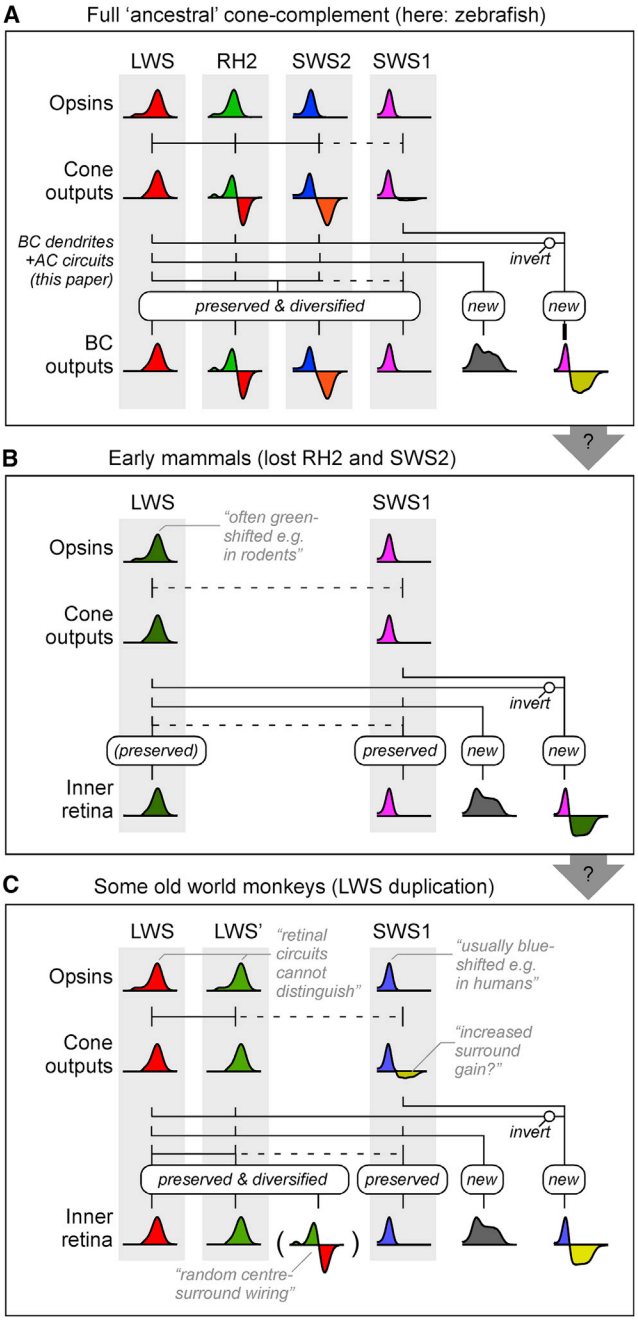

Figure 7. Possible links across vertebrate retinal color circuits

Conceptual summary schematics of retinal circuits for color vision in zebrafish (A); dichromatic mammals, such as many rodents (B); and some trichromatic old-world monkeys, such as humans (C). The colored "graphs" indicate approximate spectral tuning functions of retinal neurons in a given layer, as indicated.

and how such information can be differentially read out by downstream circuits and used to inform behavior remains unknown.

Three axes of spectral opponency

In principle, the four spectral cone types of larval zebrafish could be functionally wired for tetrachromatic vision. This would require that all four cone types contribute independently to color vision. Theory predicts that efficient coding of color should be based on four channels, an achromatic channel with no zero crossings on the spectral axis and three chromatic opponent channels with one, two, and three zero crossings, respectively.[5,47] However, such a coding strategy is not essential, as demonstrated by the trichromatic visual system of many old-world monkeys, which is based on two axes of opponency (blue-yellow and red-green), each with a single zero crossing. In the present study, we find that, among zebrafish BCs, three zero crossings predominate (Figures 5M, 5N, and 7A). Here, the single BC cluster with two zero crossings (C_7) did not set up any notable additional spectral crossings either but instead crossed once in the "blue-cone position" and once again near the "UV-red opponent position" (Figure 5K). Nevertheless, our findings support the notion that, at least at the level of BCs and under the stimulus conditions used in this study, the zebrafish visual system is capable of supporting tetrachromatic color vision, as observed behaviorally in goldfish.[48] Whether and how the larval zebrafish BCs' axes are preserved, diversified, or even lost in downstream circuits will be important to explore in the future. In this regard, both retinal ganglion cells[21,22] and brain circuits[21,49] do carry diverse spectral signals; however, beyond a global overview,[29] the nature and distribution of their spectral zero crossings remain largely unexplored.

Links with mammalian SWS1:LWS opponency

Of the three spectral axes that dominate the zebrafish inner retina (Figures 5I–5N and 7A), those functionally linked with green- (RH2) and blue-cone (SWS2) circuits are unlikely to have a direct counterpart in mammals where these cone types are lost.[1,9] However, the third axis, formed by functional opposition of UV-cone circuits against red-, green-, and blue-cone circuits, may relate to one or multiple of the well-studied mammalian SWS1:LWS opponent circuits (Figure 7B).[50,51]

Despite substantial spectral variation among both SWS1 and LWS cone types across species, mammals usually oppose the signals from SWS1 cones with those of LWS cones at a retinal circuit level.[4,6,52–56] For example, in the primate outer retina, SWS1 cones exhibit horizontal-cell-mediated spectral opponency to LWS signals.[57] Likewise, in the inner retina, signals from a highly conserved SWS1-exclusive On BC are combined with those of LWS-biased Off circuits in most, if not all, mammals that have been studies at this level.[36,51,58,59] Further such circuit motifs can involve diverse but specific types of amacrine and/or retinal ganglion cells.[4,54,60]

Several of these mammalian motifs may have a direct counterpart in zebrafish. For example, like primate SWS1 cones, also zebrafish SWS1 cones exhibit weak but significant long-wavelength opponency that is mediated by horizontal cells.[27] Beyond this possible outer retinal connection, the inferred UV:R/G/B organization in zebrafish BCs (Figures 5E, 5K, and 6) is reminiscent of mammalian circuits associated with SWS1 BCs.

First, as in most mammals,[52] $SWS1_{On}$:LWS_{Off} signals numerically dominate in zebrafish compared to $SWS1_{Off}$:LWS_{On} signals. Second, zebrafish SWS1:LWS opponent signals are predominately found in the lower-most (GCL-adjacent) fraction of the IPL (Figures 3 and 6), the same place where mammalian

SWS1-On BCs stratify.[36] Third, many zebrafish $SWS1_{On}$:LWS_{Off} signals occurred ventro-temporally (Figure 3D), the retinal region that in mice exhibits the highest density of type-9 BCs,[61] their only SWS1-exclusive BC type.[36,58] While zebrafish are not known to possess an SWS1-exclusive BC,[12] they do possess several anatomical BC types that contact SWS1 cones alongside either one or both of SWS2 (blue) and RH2 cones (green).[9,12] Such BCs may conceivably become SWS1-exclusive types upon the loss of RH2 and SWS2 cones in early mammalian ancestors.

However, not everything supports a direct correspondence between mammalian and zebrafish SWS1:LWS circuits. For example, in contrast to BCs, among the dendrites of the zebrafish retinal ganglion cells, most UV-opponent signals occur above the IPL midline, near the anatomical border between the traditional On and Off layers.[22] Nevertheless, this is approximately in line with the IPL position where several of the well-studied primate SWS1:LWS ganglion cells receive LWS-biased Off inputs,[62] hinting that similar ganglion cell motifs might also exist in zebrafish. Certainly, zebrafish do possess a number of anatomical retinal ganglion cell types[22,63] that display similar stratification patterns compared to those that carry SWS1:LWS opponent signals in diverse mammals.[51,54]

A summary of the above argument, showcasing possible links between retinal circuits for color vision in cone-tetrachromatic species, such as zebrafish, to those of most non-primate mammals and of old-world monkeys, including humans, is suggested in Figures 7A–7C. In the future, it will be important to explore whether and how mammalian circuits, such as the ones carrying SWS1:LWS signals, can be more directly linked with those found in zebrafish, for example, by leveraging molecular markers across potentially homologous types of neurons.[37,64,65]

STAR★METHODS

Detailed methods are provided in the online version of this paper and include the following:

- KEY RESOURCES TABLE
- RESOURCE AVAILABILITY
  - Lead contact
  - Materials availability
  - Data and code availability
- EXPERIMENTAL MODEL AND SUBJECT DETAILS
  - Animals
- METHOD DETAILS
  - Light Stimulation
  - 2-photon calcium imaging
  - Pre-processing of 2-photon data, IPL detection and ROI placement
  - Clustering of BCs
  - Reconstruction of BC responses from cones
- QUANTIFICATION AND STATISTICAL ANALYSIS
  - Statistics

SUPPLEMENTAL INFORMATION

Supplemental information can be found online at https://doi.org/10.1016/j.cub.2021.09.047.

ACKNOWLEDGMENTS

We thank Daniel Osorio and Thomas Euler for critical feedback. The authors would also like to acknowledge support from the FENS-Kavli Network of Excellence and the EMBO YIP. Funding was provided from the Wellcome Trust (Investigator Award in Science 220277/Z20/Z to T.B.), the European Research Council (ERC-StG "NeuroVisEco" 677687 to T.B.), UKRI (BBSRC, BB/R014817/1 to T.B.), the Leverhulme Trust (PLP-2017-005 and RPG-2021-026 to T.B.), and the Lister Institute for Preventive Medicine (to T.B.).

AUTHOR CONTRIBUTIONS

Conceptualization, P.B., T.Y., and T.B.; methodology, P.B., T.Y., and F.K.J.; investigation, P.B. and T.Y.; data curation, P.B. and T.B.; writing – original draft, T.B.; writing – review & editing, T.B., T.Y., and F.K.J.; visualization, T.B. and P.B.; supervision, T.B.; project administration, T.B.; funding acquisition, T.B.

DECLARATION OF INTERESTS

The authors declare no competing interests.

Received: August 9, 2021
Revised: September 9, 2021
Accepted: September 17, 2021
Published: October 14, 2021

REFERENCES

1. Baden, T., and Osorio, D. (2019). The retinal basis of vertebrate color vision. Annu. Rev. Vis. Sci. *5*, 177–200.
2. Jacobs, G.H. (1996). Primate photopigments and primate color vision. Proc. Natl. Acad. Sci. USA *93*, 577–581.
3. Field, G.D., Gauthier, J.L., Sher, A., Greschner, M., Machado, T.A., Jepson, L.H., Shlens, J., Gunning, D.E., Mathieson, K., Dabrowski, W., et al. (2010). Functional connectivity in the retina at the resolution of photoreceptors. Nature *467*, 673–677.
4. Dacey, D.M. (2000). Parallel pathways for spectral coding in primate retina. Annu. Rev. Neurosci. *23*, 743–775.
5. Buchsbaum, G., and Gottschalk, A. (1983). Trichromacy, opponent colours coding and optimum colour information transmission in the retina. Proc. R. Soc. Lond. B Biol. Sci. *220*, 89–113.
6. Dacey, D.M., and Packer, O.S. (2003). Colour coding in the primate retina: diverse cell types and cone-specific circuitry. Curr. Opin. Neurobiol. *13*, 421–427.
7. Pasupathy, A., Popovkina, D.V., and Kim, T. (2020). Visual functions of primate area V4. Annu. Rev. Vis. Sci. *6*, 363–385.
8. Jacobs, G.H., and Rowe, M.P. (2004). Evolution of vertebrate colour vision. Clin. Exp. Optom. *87*, 206–216.
9. Baden, T. (2021). Circuit mechanisms for colour vision in zebrafish. Curr. Biol. *31*, R807–R820.
10. Meier, A., Nelson, R., and Connaughton, V.P. (2018). Color processing in zebrafish retina. Front. Cell. Neurosci. *12*, 327.
11. Musilova, Z., Salzburger, W., and Cortesi, F. (2021). The visual opsin gene repertoires of teleost fishes: evolution, ecology, and function. Annu. Rev. Cell Dev. Biol. Published August 5, 2021. https://doi.org/10.1146/annurev-cellbio-120219-024915.
12. Li, Y.N., Tsujimura, T., Kawamura, S., and Dowling, J.E. (2012). Bipolar cell-photoreceptor connectivity in the zebrafish (Danio rerio) retina. J. Comp. Neurol. *520*, 3786–3802.
13. Li, Y.N., Matsui, J.I., and Dowling, J.E. (2009). Specificity of the horizontal cell-photoreceptor connections in the zebrafish (Danio rerio) retina. J. Comp. Neurol. *516*, 442–453.
14. Klaassen, L.J., de Graaff, W., van Asselt, J.B., Klooster, J., and Kamermans, M. (2016). Specific connectivity between photoreceptors

and horizontal cells in the zebrafish retina. J. Neurophysiol. *116*, 2799–2814.

15. Yamagata, M., Yan, W., and Sanes, J.R. (2021). A cell atlas of the chick retina based on single-cell transcriptomics. eLife *10*, 1–39.
16. Günther, A., Dedek, K., Haverkamp, S., Irsen, S., Briggman, K.L., and Mouritsen, H. (2021). Double cones and the diverse connectivity of photoreceptors and bipolar cells in an avian retina. J. Neurosci. *41*, 5015–5028.
17. Seifert, M., Baden, T., and Osorio, D. (2020). The retinal basis of vision in chicken. Semin. Cell Dev. Biol. *106*, 106–115.
18. Rocha, F.A.F., Saito, C.A., Silveira, L.C.L., de Souza, J.M., and Ventura, D.F. (2008). Twelve chromatically opponent ganglion cell types in turtle retina. Vis. Neurosci. *25*, 307–315.
19. Zimmermann, M.J.Y., Nevala, N.E., Yoshimatsu, T., Osorio, D., Nilsson, D.-E., Berens, P., and Baden, T. (2018). Zebrafish differentially process color across visual space to match natural scenes. Curr. Biol. *28*, 2018–2032.e5.
20. Daw, N.W. (1968). Colour-coded ganglion cells in the goldfish retina: extension of their receptive fields by means of new stimuli. J. Physiol. *197*, 567–592.
21. Guggiana Nilo, D.A., Riegler, C., Hübener, M., and Engert, F. (2021). Distributed chromatic processing at the interface between retina and brain in the larval zebrafish. Curr. Biol. *31*, 1945–1953.e5.
22. Zhou, M., Bear, J., Roberts, P.A., Janiak, F.K., Semmelhack, J., Yoshimatsu, T., and Baden, T. (2020). Zebrafish retinal ganglion cells asymmetrically encode spectral and temporal information across visual space. Curr. Biol. *30*, 2927–2942.e7.
23. Torvund, M.M., Ma, T.S., Connaughton, V.P., Ono, F., and Nelson, R.F. (2017). Cone signals in monostratified and bistratified amacrine cells of adult zebrafish retina. J. Comp. Neurol. *525*, 1532–1557.
24. Kamermans, M., van Dijk, B.W., and Spekreijse, H. (1991). Color opponency in cone-driven horizontal cells in carp retina. Aspecific pathways between cones and horizontal cells. J. Gen. Physiol. *97*, 819–843.
25. Kamar, S., Howlett, M.H.C., and Kamermans, M. (2019). Silent-substitution stimuli silence the light responses of cones but not their output. J. Vis. *19*, 14.
26. Connaughton, V.P., and Nelson, R. (2010). Spectral responses in zebrafish horizontal cells include a tetraphasic response and a novel UV-dominated triphasic response. J. Neurophysiol. *104*, 2407–2422.
27. Yoshimatsu, T., Bartel, P., Schröder, C., Janiak, F.K., St-Pierre, F., Berens, P., and Baden, T. (2021). Ancestral circuits for vertebrate colour vision emerge at the first retinal synapse. bioRxiv. https://doi.org/10.1101/2020.10.26.356089.
28. Euler, T., Haverkamp, S., Schubert, T., and Baden, T. (2014). Retinal bipolar cells: elementary building blocks of vision. Nat. Rev. Neurosci. *15*, 507–519.
29. Bartel, P., Janiak, F.K., Osorio, D., and Baden, T. (2021). Colourfulness as a possible measure of object proximity in the larval zebrafish brain. Curr. Biol. *31*, R235–R236.
30. Rosa, J.M., Ruehle, S., Ding, H., and Lagnado, L. (2016). Crossover inhibition generates sustained visual responses in the inner retina. Neuron *90*, 308–319.
31. Dreosti, E., Odermatt, B., Dorostkar, M.M., and Lagnado, L. (2009). A genetically encoded reporter of synaptic activity in vivo. Nat. Methods *6*, 883–889.
32. Janiak, F.K., Bartel, P., Bale, M., Yoshimatsu, T., Komulainen, E.H., Zhou, M., Staras, K., Prieto-Godino, L.L., Euler, T., Maravall, M., et al. (2019). Divergent excitation two photon microscopy for 3D random access mesoscale imaging at single cell resolution. bioRxiv. https://doi.org/10.1101/821405.
33. Belušič, G., Ilić, M., Meglič, A., and Pirih, P. (2016). A fast multispectral light synthesiser based on LEDs and a diffraction grating. Sci. Rep. *6*, 32012.
34. Baden, T., Berens, P., Franke, K., Román Rosón, M., Bethge, M., and Euler, T. (2016). The functional diversity of retinal ganglion cells in the mouse. Nature *529*, 345–350.
35. Franke, K., Berens, P., Schubert, T., Bethge, M., Euler, T., and Baden, T. (2017). Inhibition decorrelates visual feature representations in the inner retina. Nature *542*, 439–444.
36. Behrens, C., Schubert, T., Haverkamp, S., Euler, T., and Berens, P. (2016). Connectivity map of bipolar cells and photoreceptors in the mouse retina. eLife *5*, 1206–1217.
37. Shekhar, K., Lapan, S.W., Whitney, I.E., Tran, N.M., Macosko, E.Z., Kowalczyk, M., Adiconis, X., Levin, J.Z., Nemesh, J., Goldman, M., et al. (2016). Comprehensive classification of retinal bipolar neurons by single-cell transcriptomics. Cell *166*, 1308–1323.e30.
38. Connaughton, V.P., Graham, D., and Nelson, R. (2004). Identification and morphological classification of horizontal, bipolar, and amacrine cells within the zebrafish retina. J. Comp. Neurol. *477*, 371–385.
39. Connaughton, V.P., and Nelson, R. (2000). Axonal stratification patterns and glutamate-gated conductance mechanisms in zebrafish retinal bipolar cells. J. Physiol. *524*, 135–146.
40. Connaughton, V.P., and Maguire, G. (1998). Differential expression of voltage-gated K+ and Ca2+ currents in bipolar cells in the zebrafish retinal slice. Eur. J. Neurosci. *10*, 1350–1362.
41. Behrens, C., Zhang, Y., Yadav, S.C., Haverkamp, S., Irsen, S., Korympidou, M., Schaedler, A., Dedek, K., Smith, R., Euler, T., et al. (2019). Retinal horizontal cells use different synaptic sites for global feedforward and local feedback signaling. bioRxiv. https://doi.org/10.1101/780031.
42. Westheimer, G. (2007). The ON-OFF dichotomy in visual processing: from receptors to perception. Prog. Retin. Eye Res. *26*, 636–648.
43. DeVries, S.H., Li, W., and Saszik, S. (2006). Parallel processing in two transmitter microenvironments at the cone photoreceptor synapse. Neuron *50*, 735–748.
44. Baden, T., Berens, P., Bethge, M., and Euler, T. (2013). Spikes in mammalian bipolar cells support temporal layering of the inner retina. Curr. Biol. *23*, 48–52.
45. Roska, B., and Werblin, F. (2001). Vertical interactions across ten parallel, stacked representations in the mammalian retina. Nature *410*, 583–587.
46. Matsumoto, A., Briggman, K.L., and Yonehara, K. (2019). Spatiotemporally asymmetric excitation supports mammalian retinal motion sensitivity. Curr. Biol. *29*, 3277–3288.e5.
47. Atick, J.J., Li, Z., and Redlich, A.N. (1992). Understanding retinal color coding from first principles. Neural Comput. *4*, 559–572.
48. Neumeyer, C. (1992). Tetrachromatic color vision in goldfish: evidence from color mixture experiments. J. Comp. Physiol. A *171*, 639–649.
49. Fornetto, C., Tiso, N., Pavone, F.S., and Vanzi, F. (2020). Colored visual stimuli evoke spectrally tuned neuronal responses across the central nervous system of zebrafish larvae. BMC Biol. *18*, 172.
50. Neitz, J., and Neitz, M. (2017). Evolution of the circuitry for conscious color vision in primates. Eye (Lond.) *31*, 286–300.
51. Marshak, D.W., and Mills, S.L. (2014). Short-wavelength cone-opponent retinal ganglion cells in mammals. Vis. Neurosci. *31*, 165–175.
52. Jacobs, G.H. (1993). The distribution and nature of colour vision among the mammals. Biol. Rev. Camb. Philos. Soc. *68*, 413–471.
53. Chen, S., and Li, W. (2012). A color-coding amacrine cell may provide a blue-off signal in a mammalian retina. Nat. Neurosci. *15*, 954–956.
54. Mills, S.L., Tian, L.-M., Hoshi, H., Whitaker, C.M., and Massey, S.C. (2014). Three distinct blue-green color pathways in a mammalian retina. J. Neurosci. *34*, 1760–1768.
55. Szatko, K.P., Korympidou, M.M., Ran, Y., Berens, P., Dalkara, D., Schubert, T., Euler, T., and Franke, K. (2020). Neural circuits in the mouse retina support color vision in the upper visual field. Nat. Commun. *11*, 3481.
56. Khani, M.H., and Gollisch, T. (2021). Linear and nonlinear chromatic integration in the mouse retina. Nat. Commun. *12*, 1900.

57. Packer, O.S., Verweij, J., Li, P.H., Schnapf, J.L., and Dacey, D.M. (2010). Blue-yellow opponency in primate S cone photoreceptors. J. Neurosci. *30*, 568–572.

58. Breuninger, T., Puller, C., Haverkamp, S., and Euler, T. (2011). Chromatic bipolar cell pathways in the mouse retina. J. Neurosci. *31*, 6504–6517.

59. Dacey, D.M., and Lee, B.B. (1994). The 'blue-on' opponent pathway in primate retina originates from a distinct bistratified ganglion cell type. Nature *367*, 731–735.

60. Ghosh, K.K., and Grünert, U. (1999). Synaptic input to small bistratified (blue-ON) ganglion cells in the retina of a new world monkey, the marmoset Callithrix jacchus. J. Comp. Neurol. *413*, 417–428.

61. Nadal-Nicolás, F.M., Kunze, V.P., Ball, J.M., Peng, B.T., Krishnan, A., Zhou, G., Dong, L., and Li, W. (2020). True S-cones are concentrated in the ventral mouse retina and wired for color detection in the upper visual field. eLife *9*, 1–30.

62. Calkins, D.J., Tsukamoto, Y., and Sterling, P. (1998). Microcircuitry and mosaic of a blue-yellow ganglion cell in the primate retina. J. Neurosci. *18*, 3373–3385.

63. Robles, E., Laurell, E., and Baier, H. (2014). The retinal projectome reveals brain-area-specific visual representations generated by ganglion cell diversity. Curr. Biol. *24*, 2085–2096.

64. Peng, Y.-R., Shekhar, K., Yan, W., Herrmann, D., Sappington, A., Bryman, G.S., van Zyl, T., Do, M.T.H., Regev, A., and Sanes, J.R. (2019). Molecular classification and comparative taxonomics of foveal and peripheral cells in primate retina. Cell *176*, 1222–1237.e22.

65. Kölsch, Y., Hahn, J., Sappington, A., Stemmer, M., Fernandes, A.M., Helmbrecht, T.O., Lele, S., Butrus, S., Laurell, E., Arnold-Ammer, I., et al. (2021). Molecular classification of zebrafish retinal ganglion cells links genes to cell types to behavior. Neuron *109*, 645–662.e9.

66. Baden, T., Bartel, P., Yoshimatsu, T., and Janiak, F. (2021). Dataset: spectral inference reveals principal cone-integration rules of the zebrafish inner retina. Dryad Dataset.

67. Yoshimatsu, T., D'Orazi, F.D., Gamlin, C.R., Suzuki, S.C., Suli, A., Kimelman, D., Raible, D.W., and Wong, R.O. (2016). Presynaptic partner selection during retinal circuit reassembly varies with timing of neuronal regeneration in vivo. Nat. Commun. *7*, 10590.

68. Kwan, K.M., Fujimoto, E., Grabher, C., Mangum, B.D., Hardy, M.E., Campbell, D.S., Parant, J.M., Yost, H.J., Kanki, J.P., and Chien, C.-B. (2007). The Tol2kit: a multisite gateway-based construction kit for Tol2 transposon transgenesis constructs. Dev. Dyn. *236*, 3088–3099.

69. Dana, H., Sun, Y., Mohar, B., Hulse, B.K., Kerlin, A.M., Hasseman, J.P., Tsegaye, G., Tsang, A., Wong, A., Patel, R., et al. (2019). High-performance calcium sensors for imaging activity in neuronal populations and microcompartments. Nat. Methods *16*, 649–657.

70. Yoshimatsu, T., Schröder, C., Nevala, N.E., Berens, P., and Baden, T. (2020). Fovea-like photoreceptor specializations underlie single UV cone driven prey-capture behavior in zebrafish. Neuron *107*, 320–337.e6.

71. Euler, T., Franke, K., and Baden, T. (2019). Studying a light sensor with light: multiphoton imaging in the retina. In Multiphoton Microscopy. Neuromethods, *vol 148*, E. Hartveit, ed. (Humana), pp. 225–250.

72. Zimmermann, M.J.Y., Maia Chagas, A., Bartel, P., Pop, S., Prieto-Godino, L.L., and Baden, T. (2020). LED Zappelin': an open source LED controller for arbitrary spectrum visual stimulation and optogenetics during 2-photon imaging. HardwareX *8*, e00127.

73. van der Walt, S., Schönberger, J.L., Nunez-Iglesias, J., Boulogne, F., Warner, J.D., Yager, N., Gouillart, E., and Yu, T.; scikit-image contributors (2014). scikit-image: image processing in Python. PeerJ *2*, e453.

74. Baden, T., Nikolaev, A., Esposti, F., Dreosti, E., Odermatt, B., and Lagnado, L. (2014). A synaptic mechanism for temporal filtering of visual signals. PLoS Biol. *12*, e1001972.

Please cite this article in press as: Bartel et al., Spectral inference reveals principal cone-integration rules of the zebrafish inner retina, Current Biology (2021), https://doi.org/10.1016/j.cub.2021.09.047

STAR★METHODS

KEY RESOURCES TABLE

REAGENT or RESOURCE	SOURCE	IDENTIFIER
Chemicals, peptides, and recombinant proteins		
α-bungarotoxin	Tocris	2133
Agarose low melting	FisherScientific	BP1360-100
Deposited data		
All preprocessed data including each ROI's trial-averaged response and metadata (size, position etc) as well as each ROI's 16 weights	This paper, DataDryad	https://doi.org/10.5061/dryad.wstqjq2n5
Experimental models: Organisms/strains		
Danio rerio (zebrafish): *Tg(*-1.8ctbp2:SyjGCaMP7b*)*	This paper	N/A
Recombinant DNA		
pBH-1.8ctbp2-SyjGCaMP7b-pA	This paper	N/A
pBH	Yoshimatsu et al.[67]	N/A
P5E-1.8ctbp	Kwan et al.[68]	N/A
pME-SyjGCaMP7b	Kwan et al.[68]	N/A
p3E-pA	Kwan et al.[68]	N/A
p5E-1.8ctbp	Dreosti et al.[31] and this paper	N/A
pME-SyjGCaMP7b	Dana et al.,[69] Yoshimatsu et al.,[70] and this paper	N/A
Software and algorithms		
Python 3 (Anaconda)	N/A	N/A
Igor Pro 6	Wavemetrics	N/A

RESOURCE AVAILABILITY

Lead contact

Further information and requests for resources and reagents should be directed to and will be fulfilled by the Lead Contact, Tom Baden (t.baden@sussex.ac.uk).

Materials availability

The transgenic line Tg(-1.8ctbp2:SyjGCaMP7b) used in this study is available upon request to the lead author.

Data and code availability

Pre-processed functional 2-photon imaging data and associated summary statistics is freely available on DataDryad under https://doi.org/10.5061/dryad.wstqjq2n5 [66] and via the relevant links on https://badenlab.org/resources and http://retinal-functomics.net. See also Data S1 for a graphical summary of key aspects pertaining to each BC cluster.

EXPERIMENTAL MODEL AND SUBJECT DETAILS

Animals

All procedures were performed in accordance with the UK Animals (Scientific Procedures) act 1986 and approved by the animal welfare committee of the University of Sussex. Animals were housed under a standard 14:10 day/night rhythm and fed three times a day. Animals were grown in 0.1 mM 1-phenyl-2-thiourea (Sigma, P7629) from 1 *dpf* to prevent melanogenesis. For all experiments, we used 6-7 days post fertilization (*dpf*) zebrafish (Danio rerio) larvae.

Tg(1.8ctbp2:SyGCaMP7bf) line was generated by injecting pBH-1.8ctbp2-SyjGCaMP7b-pA plasmid into single-cell stage eggs. Injected fish were out-crossed with wild-type fish to screen for founders. Positive progenies were raised to establish transgenic lines. The plasmid was made using the Gateway system (ThermoFisher, 12538120) with combinations of entry and destination plasmids as follows: pBH[67] and p5E-1.8ctbp, pME-SyjGCaMP7b, p3E-pA.[68] Plasmid p5E-1.8ctbp was generated by inserting a polymerase

Please cite this article in press as: Bartel et al., Spectral inference reveals principal cone-integration rules of the zebrafish inner retina, Current Biology (2021), https://doi.org/10.1016/j.cub.2021.09.047

chain reaction (PCR)-amplified −1.8ctbp fragment[31] into p5E plasmid and respectively. Plasmid pME-SyjGCaMP7b was generated by replacing GCaMP6f fragment with PCR-amplified jGCaMP7b[69] in pME-SyGCaMP6f[70] plasmid.

For 2-photon *in-vivo* imaging, zebrafish larvae were immobilised in 2% low melting point agarose (Fisher Scientific, BP1360-100), placed on a glass coverslip and submerged in fish water. Eye movements were prevented by injection of α-bungarotoxin (1 nL of 2 mg/ml; Tocris, Cat: 2133) into the ocular muscles behind the eye.

METHOD DETAILS

Light Stimulation

With fish mounted on their side with one eye facing upward toward the objective, light stimulation was delivered as full-field flashes from a spectrally broad liquid waveguide with a low numerical aperture (NA 0.59, 77555 Newport), positioned next to the objective at ∼45°, as described previously.[27] To image different regions in the eye, the fish was rotated each time to best illuminate the relevant patch of photoreceptors given this stimulator-geometry. The other end of the waveguide was positioned behind a collimator-focusing lens complex (Thorlabs, ACL25416U-A, LD4103) which collected the light from a diffraction grating that was illuminated by 13 spectrally distinct light-emitting diodes (LEDs, details below). After mounting but before systematic light stimulation, fish were exposed to at least 5 minutes of ''spectral noise'' (each LED independently flickering in a random sequence) to light-adapt the eye.

An Arduino Due (Arduino) and LED driver (Adafruit TCL5947) were used to control and drive the LEDs, respectively. Each LED could be individually controlled, with brightness defined via 12-bit depth pulse-width-modulation (PWM). To time-separate scanning and stimulating epochs, a global ''blanking'' signal was used to switch off all LEDs during 2P scanning but enable them during the retrace, at line-rate of 1 kHz (see also Euler et al.[71] and Zimmermann et al.[72]). The stimulator code is available at https://github.com/BadenLab/HyperspectralStimulator.

LEDs used were: Multicomp Pro: MCL053RHC, Newark: C503B-RAN-CZ0C0AA1, Roithner: B5-435-30S, Broadcom: HLMP-EL1G-130DD, Roithner: LED-545-01, TT Electronics: OVLGC0C6B9, Roithner: LED-490-06, Newark: SSL-LX5093USBC, Roithner: LED450-03, VL430-5-1, LED405-03V, VL380-5-15, XSL-360-5E. Effective LED peak spectra as measured at the sample plane were, respectively (in nm): 655, 635, 622, 592, 550, 516, 501, 464, 448, 427, 407, 381, 360 nm. Their maximal power outputs were, respectively (in μW): 1.31, 1.06, 0.96, 0.62, 1.26, 3.43, 1.47, 0.44, 3.67, 0.91, 0.24, 0.23, 0.20. From here, the first ten LEDs (655 – 427 nm) were adjusted to 0.44 μW, while the three UV-range LEDs were set to a reduced power of 0.2 μW. This relative power reduction in the UV-range was used as a compromise between presenting similar power stimulation across all LEDs, while at the same time ameliorating response-saturation in the UV-range as a result of the UV-cones' disproportionately high light sensitivity.[22,70] The same strategy was used previously to record from cones.[27]

2-photon calcium imaging

All 2-photon (2P) imaging was performed on a MOM-type 2P microscope (designed by W. Denk, MPI, Martinsried; purchased through Sutter Instruments/Science Products) equipped with a mode-locked Ti:Sapphire laser (Chameleon Vision-S, Coherent) tuned to 927 nm for SyGCaMP7b imaging. Notably, like all calcium imaging, the biosensor exhibits non-instantaneous binding and unbinding kinetics, which in effect low-pass filters the ''real'' calcium signals in BCs. We used one fluorescence detection channel (F48x573, AHF/Chroma), and a water immersion objective (W Plan-Apochromat 20x/1,0 DIC M27, Zeiss). For image acquisition, we used custom-written software (ScanM, by M. Mueller, MPI, Martinsried and T. Euler, CIN, Tuebingen) running under IGOR pro 6.3 for Windows (Wavemetrics).

All data was collected using a quasi-simultaneous triplane approach by leveraging an electrically tunable lens (ETL, EL-16-40-TC-20D, Optotune) positioned prior to the scan-mirrors. Rapid axial-jumps of ∼15 μm between scan planes (ETL settling time of < 2 ms[32]) were enabled by using a non-telecentric (nTC) optical configuration (nTC_1, 1.2 mm – see Janiak et al.[32]). This nTC optical setup is described in detail elsewhere.[32] All recordings were taken at 128 × 64 pixels/plane at 3 planes (5.2 Hz effective ''volume'' rate at 1 ms per scan line).

Pre-processing of 2-photon data, IPL detection and ROI placement

Raw fluorescence stacks were exported into a Python 3 (Anaconda) environment. The data were de-interleaved and separated into the three recording planes. Next, the data were linearly detrended, linearly interpolated to 42 Hz, and aligned in time. The anatomical borders of the inner plexiform layers were automatically detected by first median-smoothing the time standard deviation images with a Gaussian kernel size of 3 pixels. From here, every pixel above the 35% per-image amplitude threshold was registered as IPL. This automated procedure was made possible by the fact that GCaMP6f expression was restricted to the presynaptic terminals of BCs, which also defined the anatomical borders of the IPL.

To place regions of interest (ROI), a quality index (QI) as described previously[34] was calculated for each pixel. In short, the QI measures the ratio of variance shared between stimulus repetitions and within a single stimulus repetition. The larger the QI, the more variance in the trace is due to the presented stimulus:

$$QI = \frac{VarC_{rt}}{VarC_{tr}}$$

Please cite this article in press as: Bartel et al., Spectral inference reveals principal cone-integration rules of the zebrafish inner retina, Current Biology (2021), https://doi.org/10.1016/j.cub.2021.09.047

where *C* is the *T* by *R* response matrix (time samples by stimulus repetitions) and x and Var[]x denote the mean and variance across the indicated dimension, respectively. QI ranges from 0 (perfectly random) to 1 (all stimulus repetition responses are identical). This yielded "QI-images" that indicated where in a scan BC-responses were located. From here, ROIs were automatically placed using custom Python scikit-image scripts.[73] In brief, QI-images were adaptively thresholded using kernel size 5 pixels which helped accentuate responsive image structures that were approximately BC-terminal-sized (in our scan configuration, most BC-terminals were ~5 pixels in diameter – *cf.* Figure 1D). The resulting binary images were distance-transformed and shrunk. The contours of the remaining groups of pixels were recorded and filled, and the highlighted pixels were used as ROI coordinates. This yielded ROI sizes of 1.36 ± 0.17 μm^2 (mean ± SD), which is in line with anatomical sizes of BC terminals in larval zebrafish.[74] While it remains possible that a minority of ROIs over- or under-split terminals, this possible limitation was judged to be minimal based on manual inspections. The IPL position of each ROI was defined as the relative position of the center-of-mass of the filled ROI contour to the nearest inner and outer borders of the IPL.

ROI traces were converted to z-scores. For this, a 5 s portion of the trace preceding stimulus presentation was drawn and defined as baseline. The standard deviation of this baseline fluorescence signal was calculated and used to z-score the remainder of the trace. Finally, QIs as described above for each pixel were also calculated for each ROI. In line with how we previously processed the cones,[27] ROIs with QI < 0.4 were excluded from further analysis. n = 6,125 ROIs passed this quality criterion (72 triplane scans from 7 fish).

Clustering of BCs

To identify structure among the BC-dataset, trial-averaged ROI traces were PCA-transformed and clustered as described previously (e.g., Zimmermann et al.[19] and Baden et al.[34]). In brief, we used the first 48 principal components, which accounted for 82% of total variance. Of these, components that near-exclusively carried high-frequency content which is likely linked to noise were discarded. The transformed time-traces were clustered using the scikit-learn (Python 3, Anaconda) implementation of the Gaussian Mixture Models algorithm. The number of clusters (29) was determined using the Bayesian information criterion (BIC). However, the BIC curve notably flattened above ~20 clusters, suggesting that a range of solutions would be similarly plausible. Clusters were judged as stable over repeated clustering runs starting from different random seeds, in the sense that they always picked up several broadband and UV:R/G/B response types, followed by a smaller number of "cone-like" ones (*cf.* Figure 5).

Reconstruction of BC responses from cones

To reconstruct each BC-mean response into constituent spectral and temporal components, we combined the average spectral tuning curve of each of the four cone-types (from Yoshimatsu et al.[27]) with four temporal components associated with a given light response (i.e., 1.5 s On, 1.5 s Off). The four temporal components used, obtained by non-negative matrix factorization across all light responses and cluster means, resembled light-transient, light-sustained, dark-transient, and dark-sustained temporal profiles (Figure 3B). Next, each ROI's trial averaged trace was decomposed into a corresponding 4 by 10 array (four temporal components X 10 LEDs). Here, we restricted the reconstruction to the central 10 LEDs that generally elicited the greatest variance across BCs. This also avoided using responses to the shortest wavelength LED which may have driven saturating responses in UV-cones (UV-cones are more light-sensitive than the other cones). Moreover, it avoided using the two longest-wavelength LEDs where responses were comparatively weak and thus noisy.

This yielded four spectral tuning curves per ROI (i.e., light-transient x 10 LEDs, light-sustained x 10 LEDs and so on), which were then linearly interpolated to the range of 360 - 610 nm to conform with the cone data format. The BC tuning curves were then modeled as linear combinations of the cone tuning curves with a lasso regularizer, which yielded four cone weights X four response bases per BC-trace. For simplicity, we henceforth used the ROI-averaged weights within a cluster for further processing, but each ROI's individual weights are available to download from DataDryad.[66]

To assess reconstruction quality (Figure S2), reconstructed data was subtracted from the original ROI-means to yield residuals. From here, we compared original data, reconstructions, and residuals by two metrics: variance explained across all clusters, and temporal power explained. To determine the fraction of variance explained by the reconstructions, we first computed the total variance across all clusters for each time-point. The result of this process, plotted beneath each corresponding heatmap (Figure S2A), showed similar time-variance profiles across cluster means and their reconstructions (panels 1 and 2), but very little remaining signal for the residuals (panel 3). From here, we computed the area under the curve for each variance-trace and normalized each to the result from the original cluster means. By this metric, cluster reconstructions captured 94.0% of the original variance, while residuals carried 5.1%.

To determine the extent to which temporal structure was captured, we used a similar approach to the one above, however in this case based on a magnitude-squared Fourier Transform of each time-trace (Figure S2B), limiting the result between 0.16 and 2 Hz which captured the bulk of physiologically meaningful temporal components given the optical imaging approach used (i.e., lower-frequency components would mainly arise from imperfect detrending, while higher-frequency components would exceed the Nyquist recording limit, and further be limited by the kinetics of GCaMP7b. From here, we computed the average of all clusters' Fourier transforms (plotted beneath each panel) and again computed the faction of this signal captured by the reconstruction (103.8%) and residuals (3.8%). Notably, while this metric was mainly informative about low frequency components which dominated all signals, also higher frequency components were generally well captured, as visible in the individual heatmaps.

Please cite this article in press as: Bartel et al., Spectral inference reveals principal cone-integration rules of the zebrafish inner retina, Current Biology (2021), https://doi.org/10.1016/j.cub.2021.09.047

QUANTIFICATION AND STATISTICAL ANALYSIS

Statistics

No statistical methods were used to predetermine sample size. Owing to the exploratory nature of our study, we did not use randomization or blinding. To compare weight amplitude distributions (Figures 5A and 5B) we used the paired Wilcoxon Rank Sum Test, taking paired components as the input (i.e., comparing red-light-transient versus green-light-transient, and so on). To assess weight correlations between cones (Figures 5C–5E and S2), we in each case list the Pearson correlation coefficient ρ and 95% confidence intervals (CI) based on the mean weights per cluster. Individual temporal weights were not considered in this analysis. All statistical analysis was performed in Python 3 (Anaconda) and/or Igor Pro 6 (Wavemetrics).

Current Biology, Volume *31*

Supplemental Information

Spectral inference reveals principal cone-integration rules of the zebrafish inner retina

Philipp Bartel, Takeshi Yoshimatsu, Filip K. Janiak, and Tom Baden

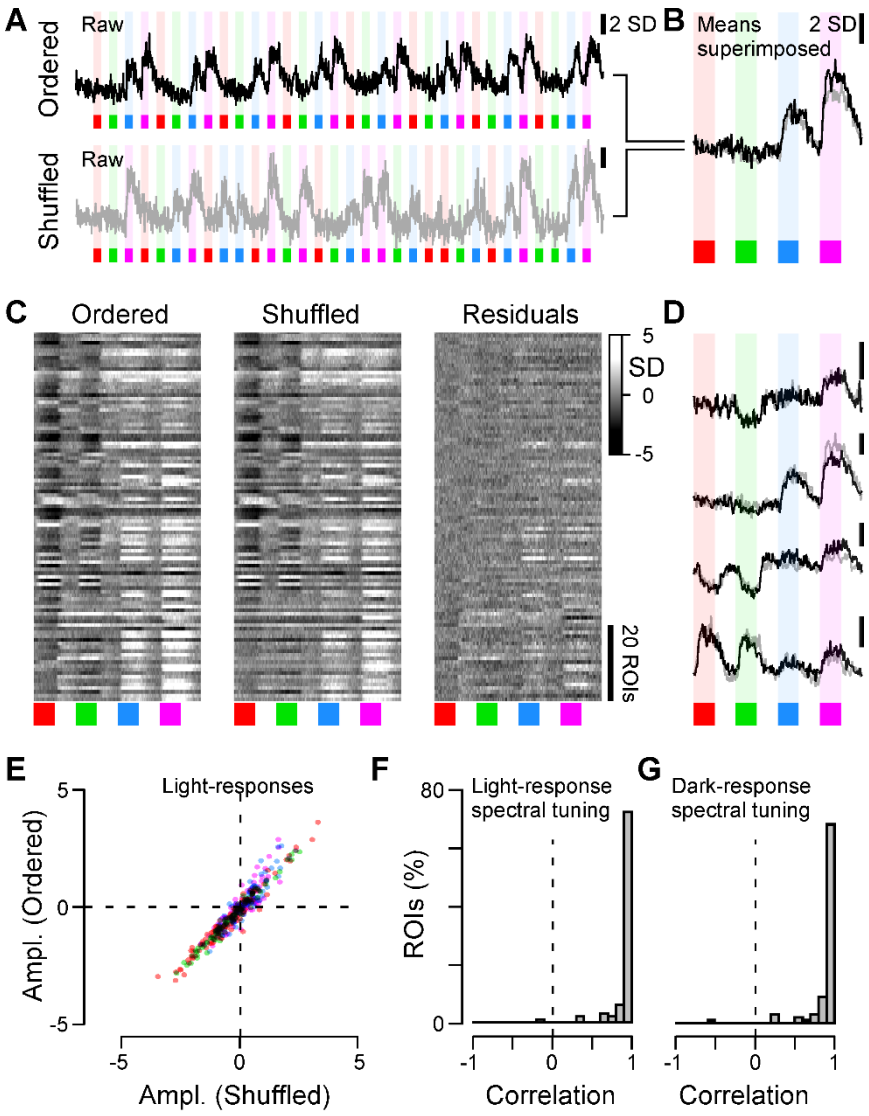

Figure S1 | Comparing responses to ordered versus pseudorandom stimulus sequences. Related to Figure 1. A,B, Example recording from a single ROI responding to four coloured flashes of light (592, 464, 427, 381 nm; 1.5 s, with 1.5 s gaps) presented either in spectral sequence (A, top, black trace, aka. “ordered”) or in pseudorandom sequence (A, bottom, grey trace, aka. “shuffled”), and their stimulus-aligned averages superimposed (B). Note that to facilitate direct comparison, the average flash responses to the pseudorandomised stimulus were concatenated in spectral sequence to resemble the means of the ordered presentation. **C**, Heatmaps of mean responses as in (B) from 100 ROIs (n = 2 fish, n = 3 scan fields) that passed the same quality criterion used for the more spectrally resolved dataset (Methods). Shown are all mean responses to the ordered sequence (left), to the shuffled sequence (middle), and their residuals after subtracting the shuffled from the ordered means (right). **D**, Further examples of means from ordered (black) and shuffled (grey) presentations. Note that generally, responses to both approaches were similar. **E**, Direct comparison of each ROI’s mean response amplitudes during each flash for the ordered versus shuffled condition. Flash-wavelength indicated by the four colour shadings. **F,G**, Quantification of possible differences in spectral tuning functions obtained by either method. Shown are histograms of the linear correlation coefficients between spectral tunings functions based on each ROI’s “light-responses” (F, based on E; correlation mean±SD: 0.84±0.33) and between “dark-responses” (G, i.e. based on four response amplitudes between flashes, correlation mean±SD: 0.81±0.36).

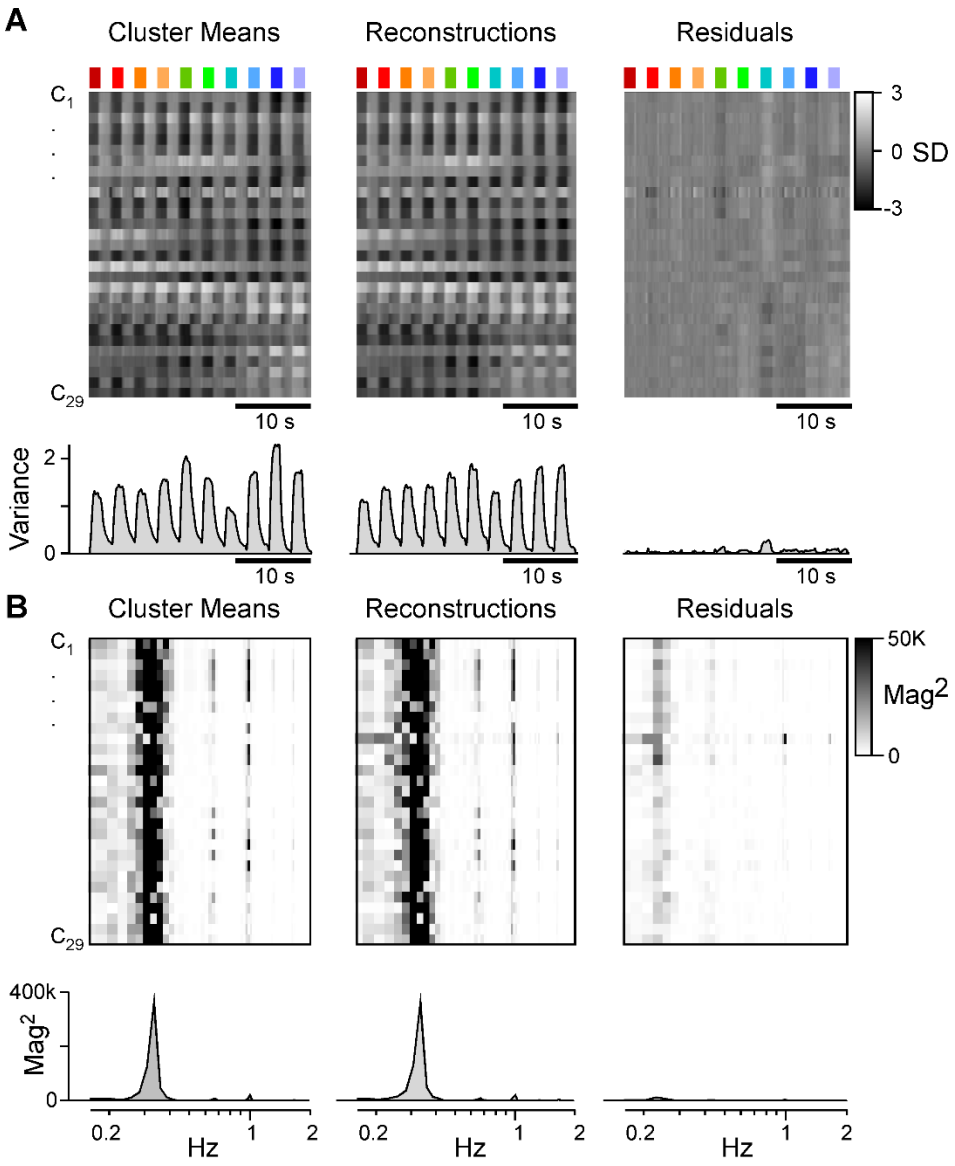

Figure S2 | Cluster reconstruction details. Related to Figure 3. A, Time-aligned heatmaps of all cluster means (left) are shown alongside their corresponding reconstructions (middle) and residuals (right). The time trace below each cluster shows the total variance across all clusters per time point (Methods). **B**, as A, but for magnitude-squared Fourier transforms of each cluster, reconstruction, and residuals. The traces below each panel show the averages of these transforms across all clusters (Methods). Note that for both (A) and (B), residuals retain only a small fraction of the original signal, indicating high reconstruction fidelity. Reconstruction quality of each individual cluster can further be assessed in Appendix 1.

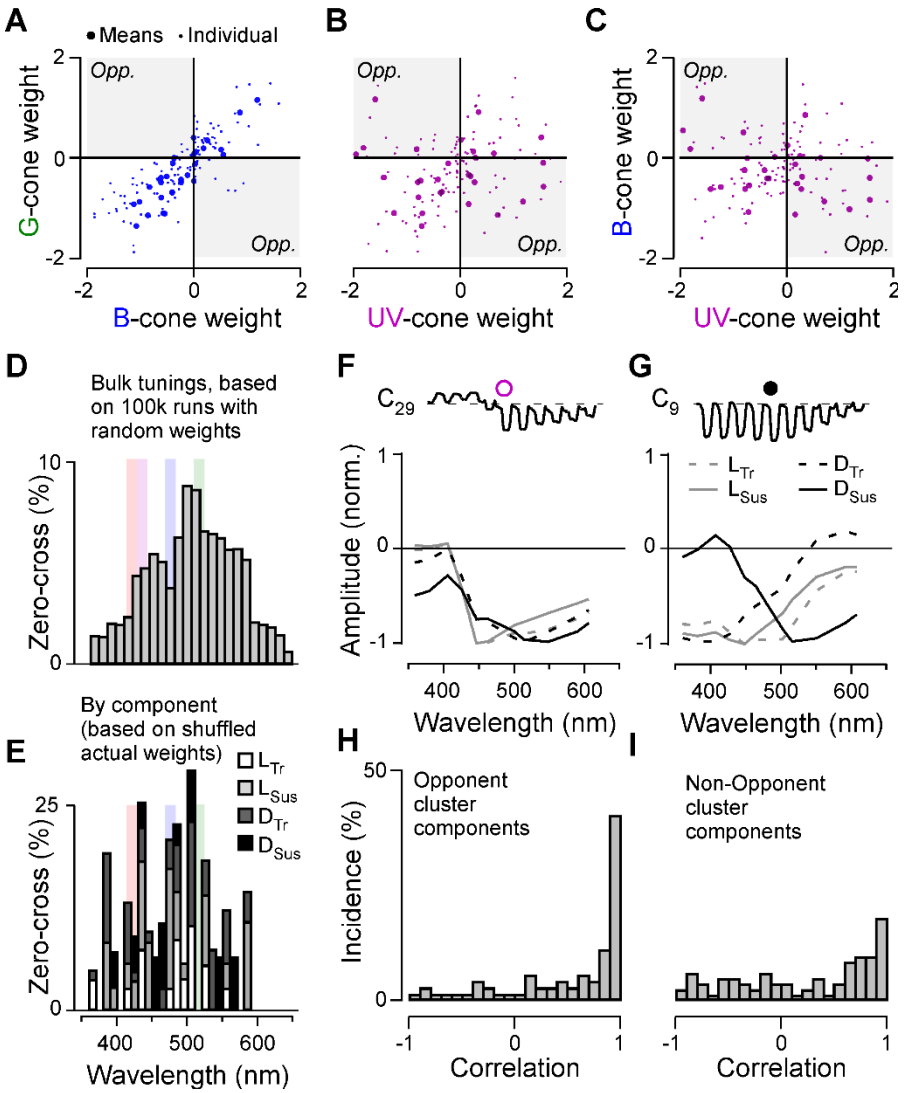

Figure S3 | Spectral tunings and temporal components. Related to Figure 5. A-C, As Figure 5C-E, but showing weight correspondences between green-blue, green-UV and blue-UV cones, respectively. **D**, As Figure 5M, but following based on 100,000 iterations using randomised values (between -5 and 5) for each of the 16 weight variables. **E**, as Figure 5N, but following random permutation of time-components across cones. **F,G**, Spectral tuning functions for two example clusters (C_{29} and C_9, respectively), computed individually by temporal components as indicated. Note that for C_{29} (F), the four tuning functions were similar to each other, while for C_9, the tuning of the dark-sustained component deviated strongly from that of the remaining three components. Corresponding time-component resolved tuning functions are detailed for each cluster in Appendix 1. **H,I**, Distribution of correlations between each cluster's "time-component spectral tuning functions" as illustrated in (F,G), for spectrally opponent clusters (H), and for non-opponent clusters (I).